The Far-IR view of PDRs and star formation

Asunción Fuente
Observatorio Astronómico Nacional (OAN-IGN, Spain)

PDR Basic model (Tielens & Hollenbach 1985, ApJ 291, 722)

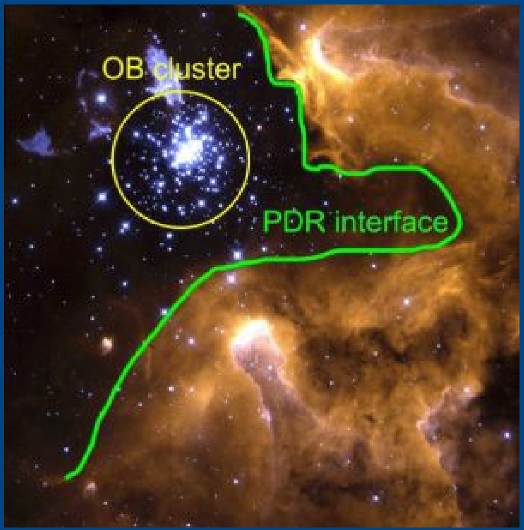

HST-WFPC2
Wolfgang Brandner (JPL/IPAC), Eva K Grebel (Univ. Washington), You-Hua Chu (Univ. illinois) and NASA

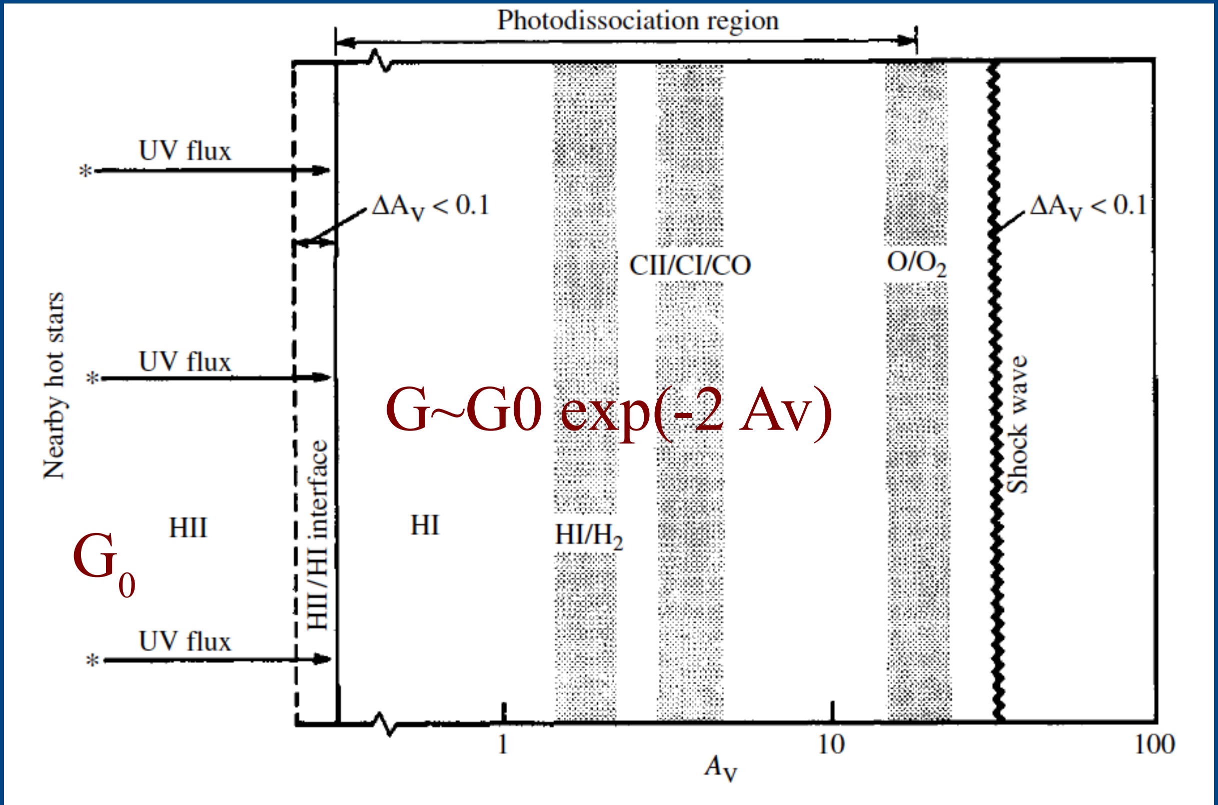

The physical /chemical conditions of a PDR depends on G_0/n and Av

H/H_2 transition at Av~2 mag

$C^+/C/CO$ transition at Av~4 mag

O/O_2 transition at Av~ 20 mag

FIR is the domain to study PDRs

i. Dust temperature > 50 K. The thermal dust emission peaks at mid-IR wavelengths.

i. The gas is partially atomic. The most important atomic cooling lines, [CII] 158μm and [OI] 63μm and 145μm, occurs in the FIR domain.

i. The most intense molecular lines in PDRs, mid- and high-J CO rotational lines, also at FIR and mid-IR frequencies.

Spitzer
3-180 μm
0.85m
2003

Herschel
60-625 μm
3.5m
2009

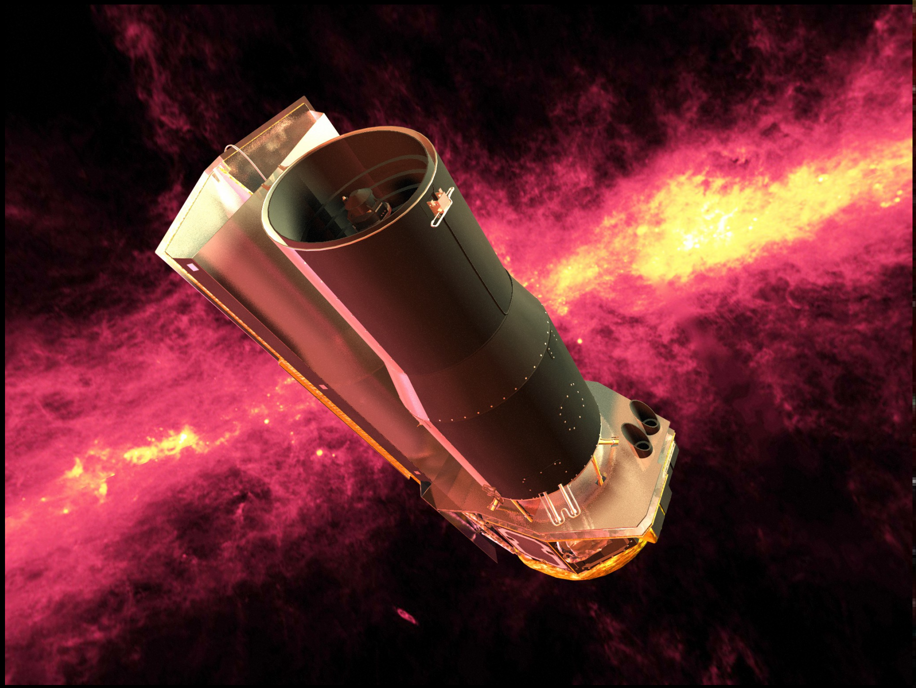

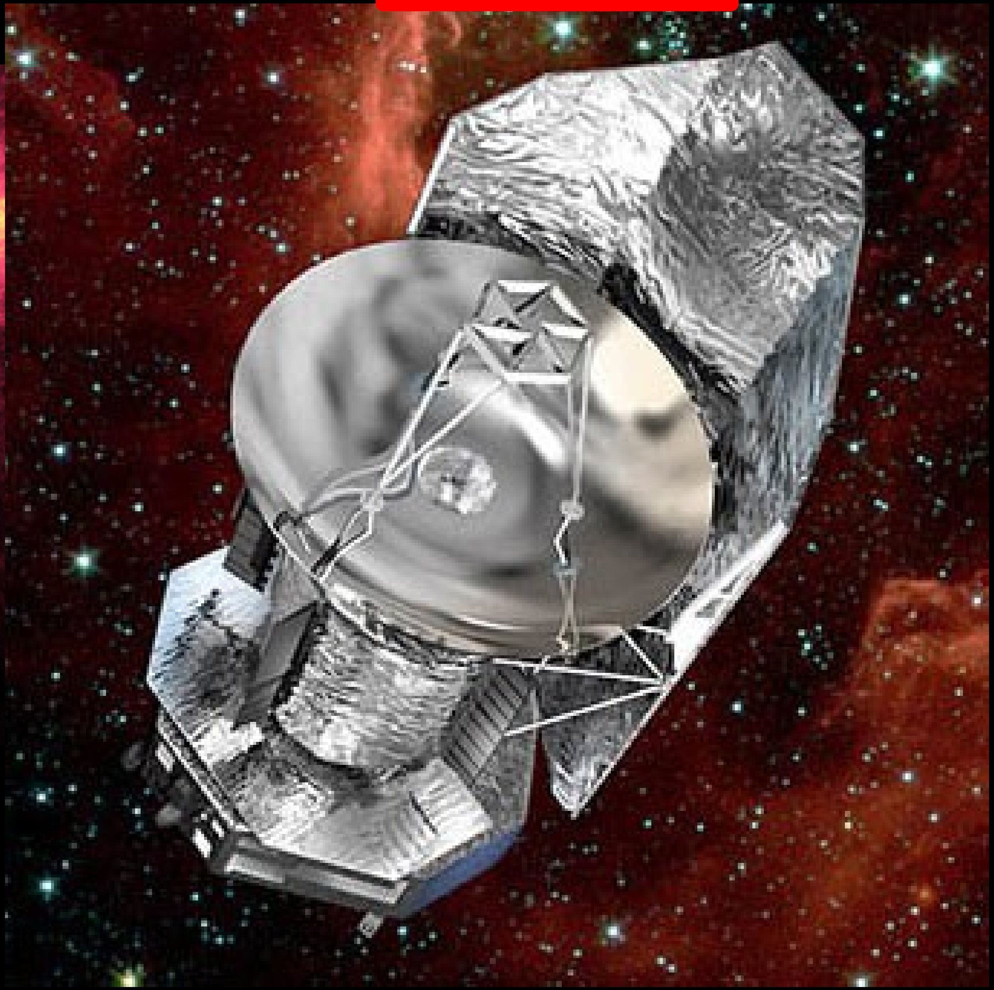

Photodissociation Regions (PDRs)

Photon dominated or photodissociation regions (PDRs) are regions where the FUV radiation dominates the energetic balance and chemistry.

i. The regions close to the O and B stars: HII regions, reflection nebulae, the surface of proto-planetary disks

ii. The surface of molecular clouds

iii. Diffuse clouds

iv. Planetary nebuale

v. The nucleus of starburst galaxies

vi. Distant galaxies?

Diffuse clouds

Probing the diffuse medium with Herschel HIFI

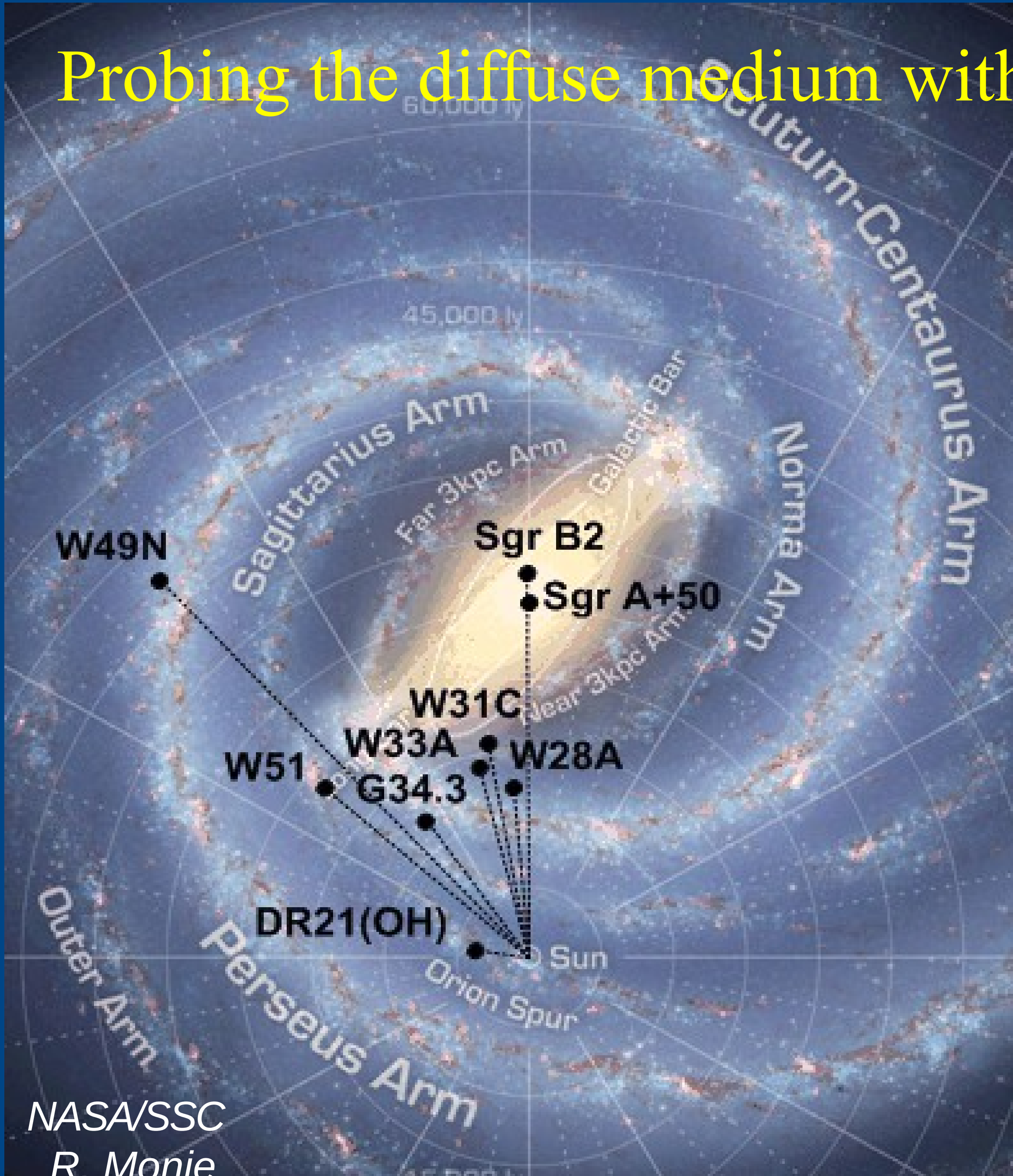

Massive star forming regions as background sources for absorption spectroscopy.

The only way to probe gas at low excitation

Accurate measurement of line profiles and opacities -> better measurement of column densities

→The PRISMAS GTKP of Herschel (*Gerin et al.*)

Why Hydrides?

-Built in the first chemical steps starting from atomic gas

-At the root of the interstellar chemistry

-Trace diffuse gas that cannot be traced by the standard tracer CO.

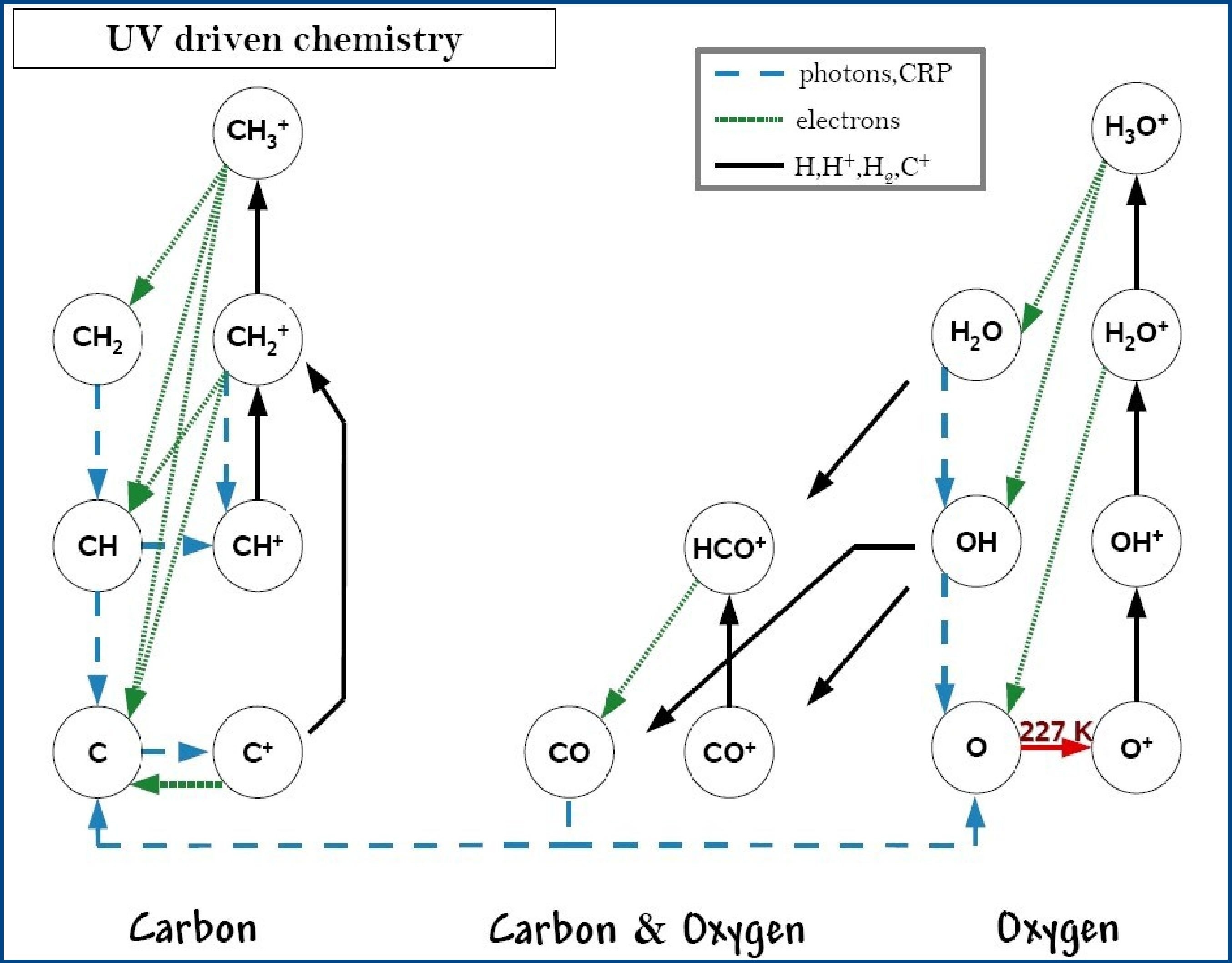

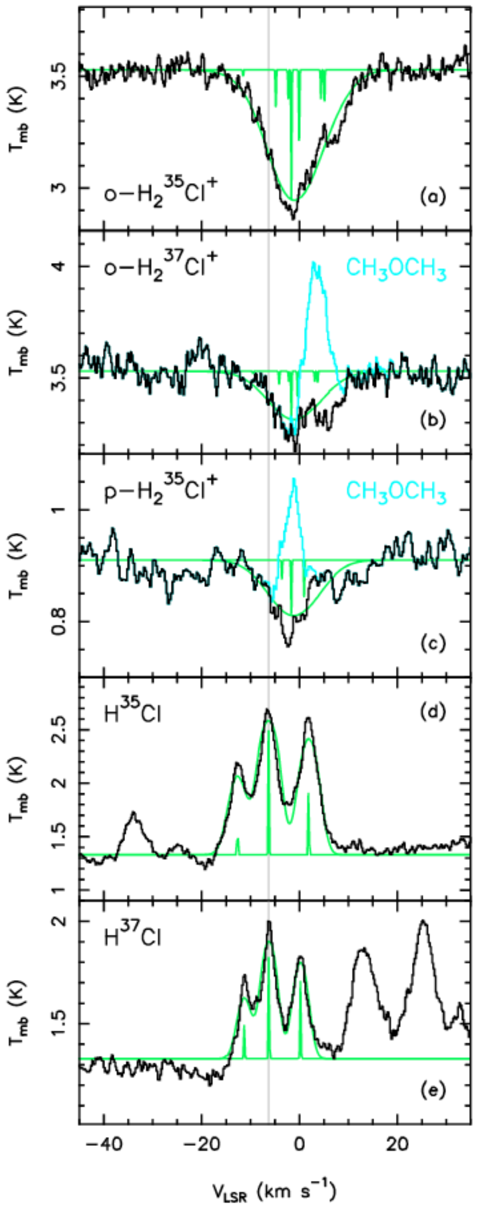

Fig. 1. Spectra of chlorine species in NGC 6334I: **a)** o-$H_2^{35}Cl^+$ $2_{12}-1_{01}$; **b)** o-$H_2^{37}Cl^+$ $2_{12}-1_{01}$, **c)** p-$H_2^{35}Cl^+$ $1_{11}-0_{00}$, **d)** $H^{35}Cl$ 1−0; and **e)** $H^{37}Cl$ 1−0. The velocity scale corresponds to the strongest HFS components. Green lines show HFS fits and positions of the HFS components. The o-$H_2^{37}Cl^+$ and p-$H_2^{35}Cl^+$ lines are blended with dimethyl ether emission (light-blue lines in panels **b)** and **c)**).

HCl^+, H_2Cl^+

Formation route:

$$Cl^+ + H_2 \rightarrow HCl^+ + H.$$

$$HCl^+ + H_2 \rightarrow H_2Cl^+ + H.$$

$[HCl]/[H_2Cl^+]$~1 -10 in agreement with PDR chemical models

HCl and H_2Cl^+ column densities in excess of model predictions

De Luca et al., 2012, ApJ 751, L37; Lis et al. 2010, A&A 521, L9

HF, CH^+,SH^+,OH^+,H_2O^+ toward G10.6-0.4

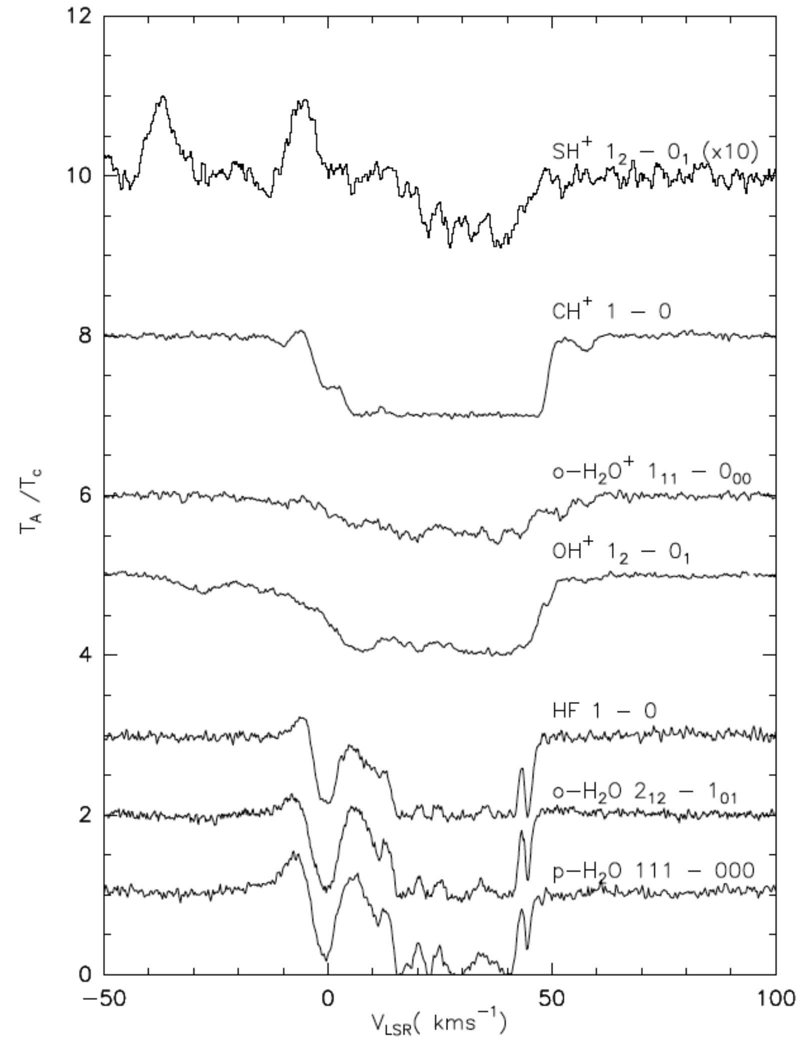

Fig. 1. Absorption of the ground-state rotational transitions of six light hydrides observed against the dust continuum emission of the bright star-forming region W31C (or G10.6-0.34) by Herschel/HIFI. The emission lines in the SH^+ spectrum are methanol lines from the star-forming region.

OH^+ and H_2O^+ consistent with predictions of gas phase chemical models.

$N(OH^+)/N(H_2O^+)<4$ ->Only a small fraction of the gas (<10%) is in molecular form.

The high abundances of CH^+ and SH^+ are only understood in the context of turbulent models.

Gerin et al. 2010, A&A 518, L110; Falgarone et al., SF2A 2010

Herschel HIFI: using HF to trace H_2

$$F + H_2 \rightarrow HF + F + 1.4\ \text{eV}$$

HF is present as soon as H_2 is present, even in clouds with no detectable CO or H_2O.

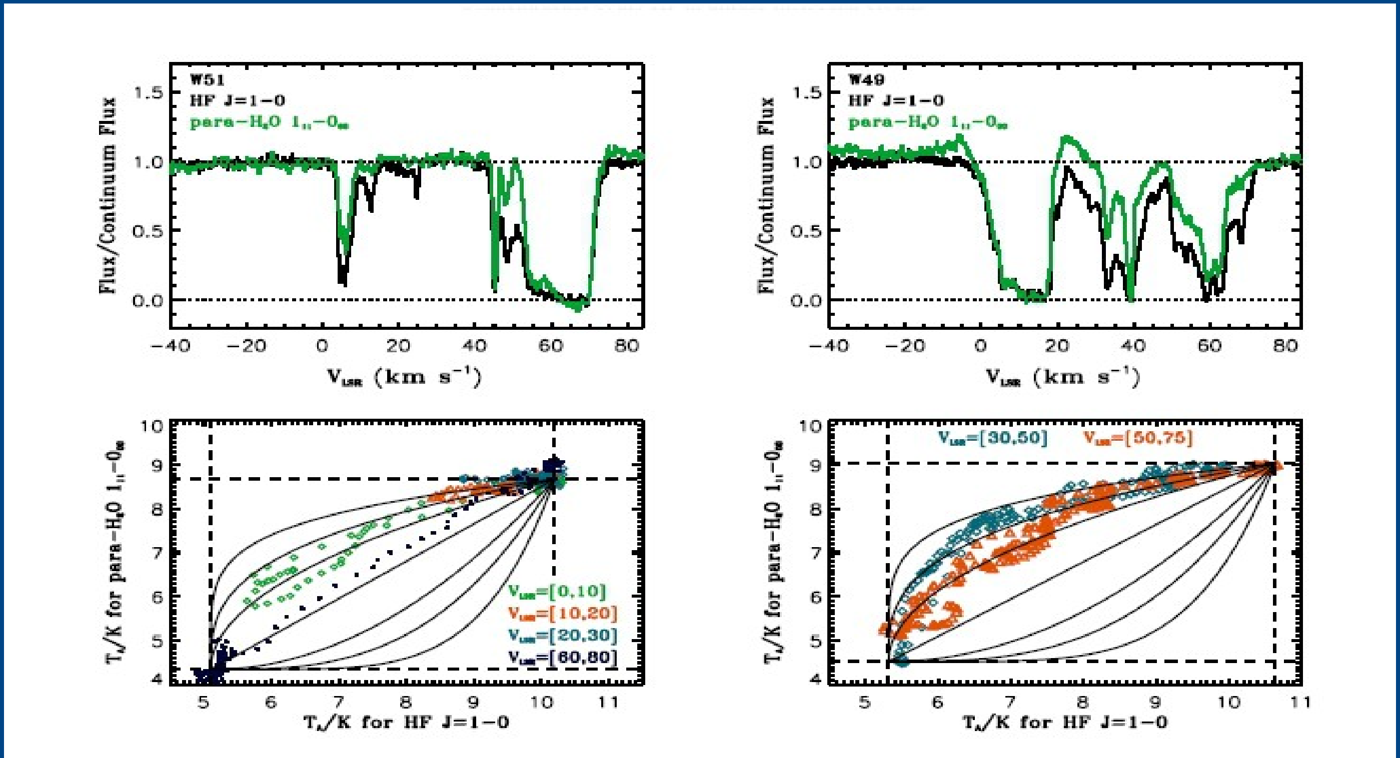

HF 1232 GHz

p-H_2O 1113 GHz

Neufeld et al. 2010, Sonnentrucker et al. 2010 & 2012 subm., Monje et al. 2011

Star forming regions (gas)

PDR Basic model (Tielens & Hollenbach 1985, ApJ 291, 722)

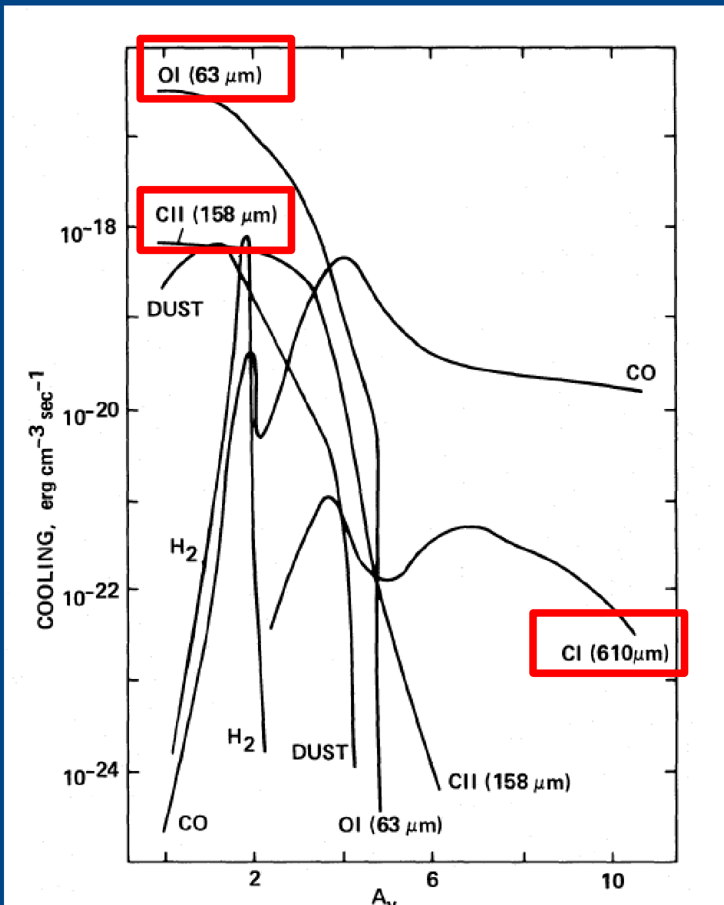

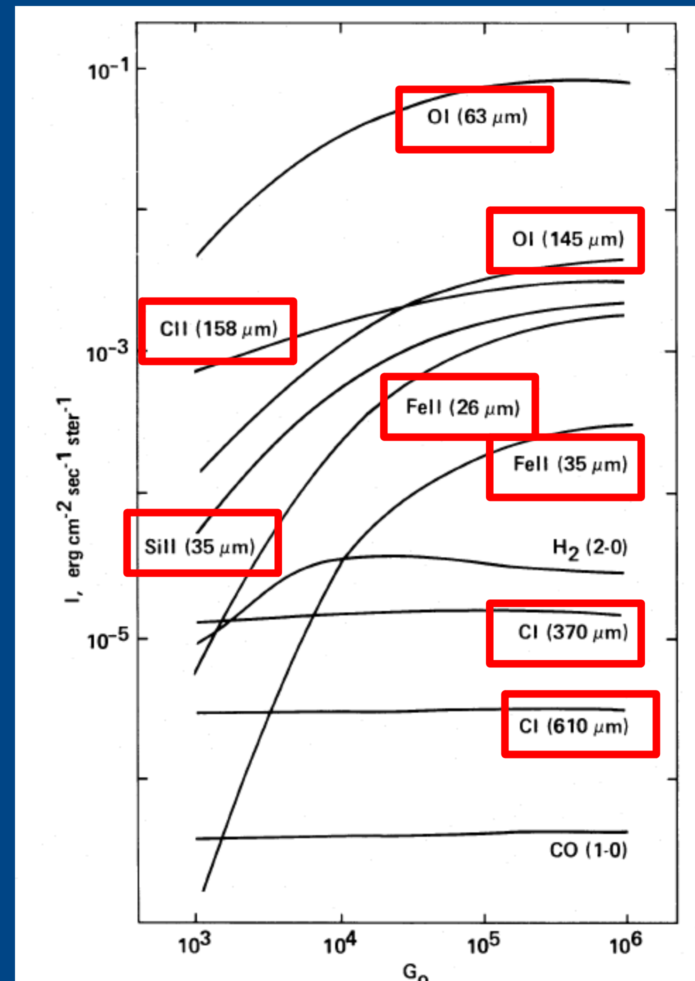

$n=2\text{x}10^5\ \text{cm}^{-3}$

D=400 pc

20 mag → 0.03 pc → 17 arcsec

Partially atomic layer

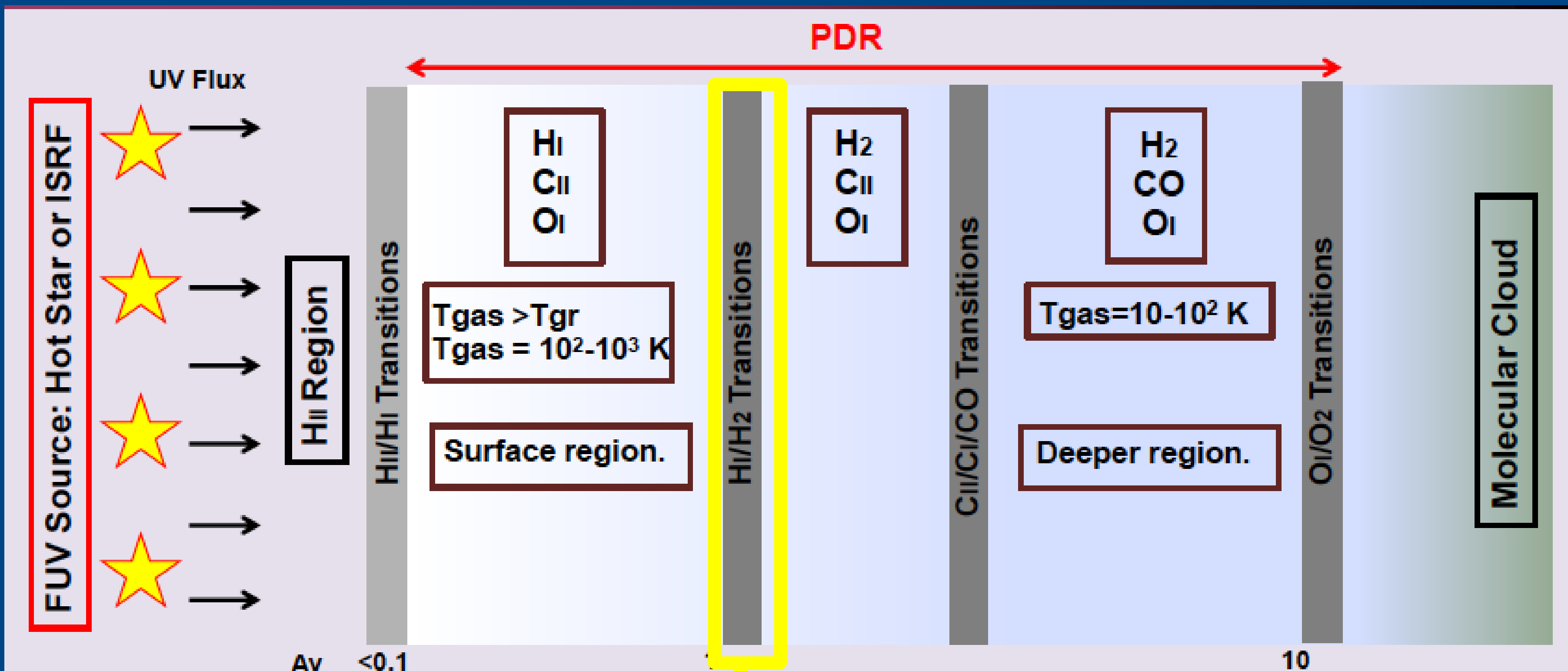

$OH, CH, OH^+, CH^+, SH^+, HF, H_2Cl^+, HCl^+$

Orion Bar: CH^+, SH^+

Transition	Frequency (MHz)	E_{up} (K)	A (s^{-1})	Instrument/band	Beam-size ($''$)	η_{mb}
CH^+ 1–0	835 137.5	40.1	6.36×10^{-3}	HIFI, band 3a	26.5	0.75
CH^+ 2–1	1 669 281.3	120.2	6.10×10^{-2}	HIFI, band 6b	15.0	0.72
CH^+ 3–2	2 501 440.5	240.2	2.20×10^{-1}	PACS	9.4[1]	
CH^+ 4–3	3 330 629.7	400.1	5.38×10^{-1}	PACS	9.4[1]	
CH^+ 5–4	4 155 872.0	599.5	1.07	PACS	9.4[1]	
CH^+ 6–5	4 976 201.4	838.3	1.86	PACS	9.4[1]	
$^{13}CH^+$ 1–0	830216.1	39.9	5.83×10^{-3}	HIFI, band 3a	26.5	0.75
SH^+ $N_J = 1_2–0_1$, $F = 3/2–1/2$	526 038.7	25.3	7.99×10^{-4}	HIFI, band 1a	44.2	0.76
SH^+ $N_J = 1_2–0_1$, $F = 5/2–3/2$	526 047.9	25.3	9.59×10^{-4}	HIFI, band 1a	44.2	0.76
SH^+ $N_J = 1_2–0_1$, $F = 3/2–3/2$	526 124.9	25.3	1.60×10^{-4}	HIFI, band 1a	44.2	0.76
SH^+ $N_J = 1_1–0_1$, $F = 3/2–1/2$	683 336.1	32.8	2.90×10^{-4}	HIFI, band 2a	33.2	0.75
SH^+ $N_J = 1_1–0_1$, $F = 1/2–1/2$	683 362.0	32.8	1.16×10^{-3}	HIFI, band 2a	33.2	0.75
SH^+ $N_J = 1_1–0_1$, $F = 3/2–3/2$	683 422.3	32.8	1.45×10^{-3}	HIFI, band 2a	33.2	0.75
SH^+ $N_J = 1_1–0_1$, $F = 1/2–3/2$	683 448.2	32.8	5.79×10^{-4}	HIFI, band 2a	33.2	0.75
CF^+ 5–4	512 846.5	73.8	8.21×10^{-4}	HIFI, band 1a	44.2	0.76
CF^+ 6–5	615 365.6	103.4	1.44×10^{-3}	HIFI, band 1b	44.2	0.76
$^{13}CF^+$ 5–4	488 664.3	70.0	7.10×10^{-4}	HIFI, band 1a	44.2	0.76

Nagy, Z., van der Tak, F., Ossenkopf, V., et al., 2013, A&A 550, 96

CH^+, SH^+ (Meudon PDR code + excitation model)

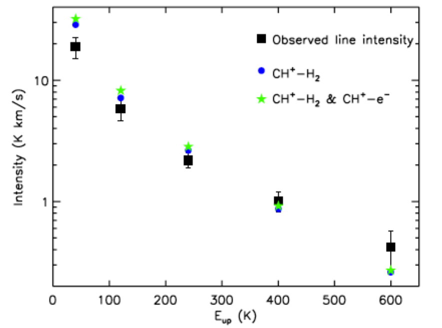

Fig. 7. Output of the RADEX models corresponding to a model with $N(CH^+) = 9 \times 10^{14}$ cm^{-2}, $n(H_2) = 10^5$ cm^{-3}, $n(e^-) = 10$ cm^{-3}, $T_{kin} = 500$ K. The blue symbols correspond to a model with excitation via collisions with H_2, the green symbols to a model with excitation via H_2 and electron collisions.

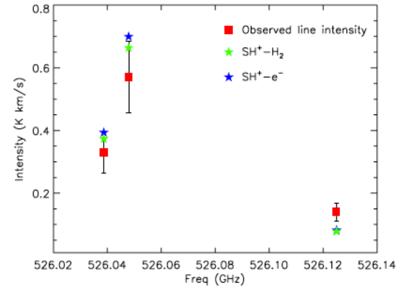

Fig. 8. Output of the RADEX models for H_2 and electron collisions compared to the observed line intensities of SH^+ for a model with $N(SH^+) = 10^{13}$ cm^{-2}, $n(H_2) = 10^6$ cm^{-3}, $n(e^-) = 10$ cm^{-3}, and $T_{kin} = 200$ K.

Collisions with e^-, H and H_2

Reactive collisions

IR pumping

Formation pumping

CH^+ and SH^+ are formed in the warm surface (Av~1.5 mag) where the gas is partially atomic. Their column densities are well predicted and CH^+ is mainly formed by reactions with vibrational excited H_2 (Agúndez et al. 2010, ApJ 713, 662; Zanchet et al. 2014, AJ 146, 125)

WHY DIFFERENT LINEWIDTHS?

Nagy, Z., van der Tak, F., Ossenkopf, V., et al., 2013, A&A 550, 96

Orion Bar: CH^+, SH^+

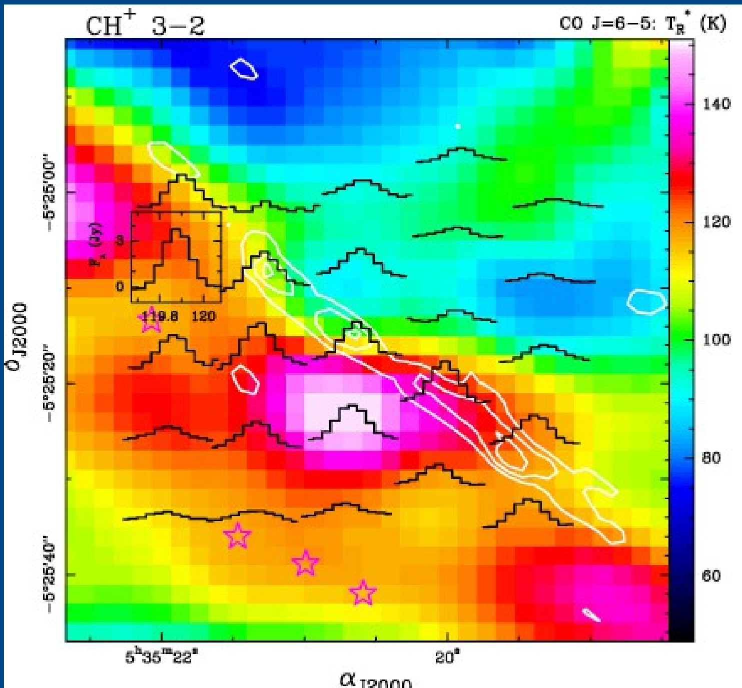

Δv~5 km/s

CH^+

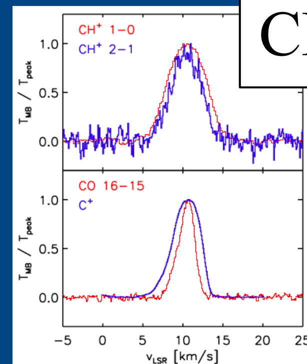

Δv~3 km/s

SH^+

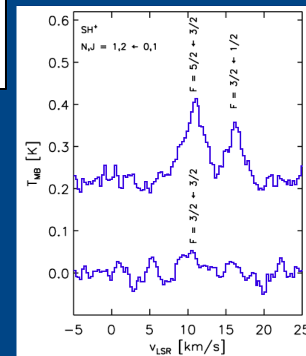

Δv~2 km/s

CF^+

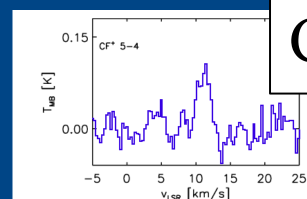

Δv~3 km/s

CO^+

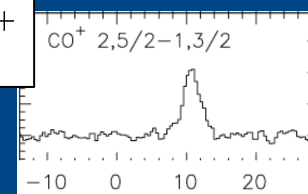

Fuente et al. 2003, A&A 406,899

The line-widths of the CH^+ 1-0 and 2-1 lines are similar to C^+ and HF, but significantly broader than SH^+, CF^+ and CO^+.

Nagy, Z., van der Tak, F., Ossenkopf, V., et al., 2013, A&A 550, 96

The ALMA view of the Orion Bar

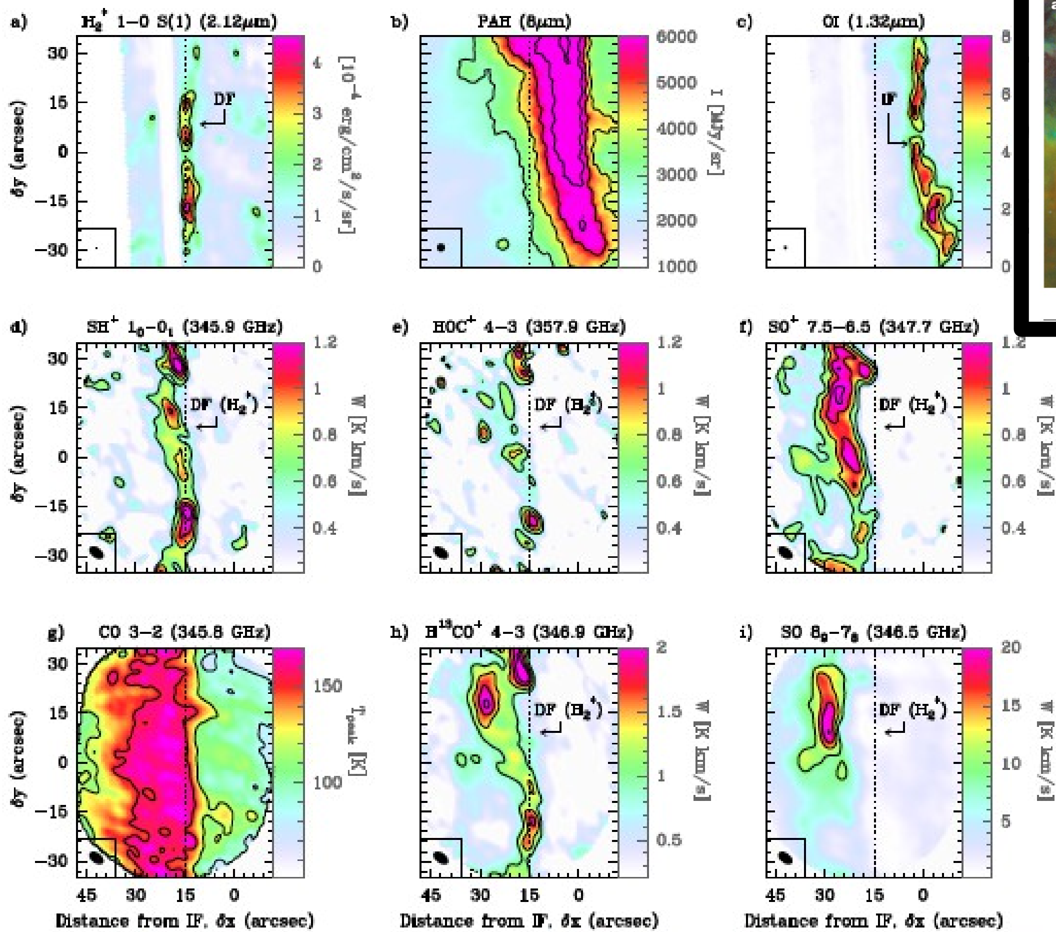

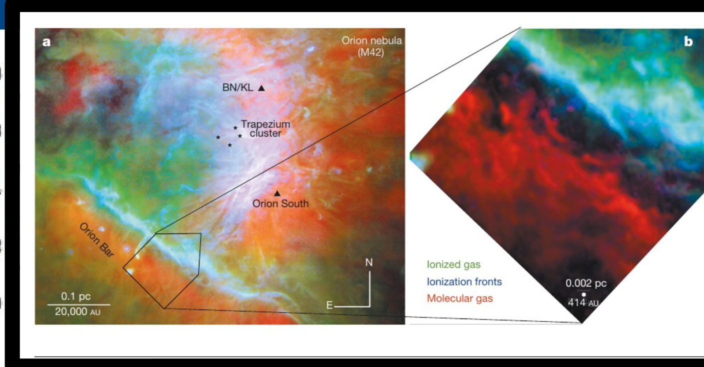

Figure 4. ALMA-ACA observations of several molecules, including the reactive ions SH^+ and HOC^+ and complementary images of the Bar (Goicoechea et al. 2017). All images have been rotated to bring the FUV illuminating direction in the horizontal direction (from the right). The upper row shows images of a) the H_2 v=1-0 $S(1)$ line at 2.12 μm, delineating the dissociation front (DF) (Walmsley et al. 2000); b) the Spitzer 8 μm emission produced mainly by PAHs, and c) the fluorescent O I 1.32μm line arising from the H II/PDR boundary (Walmsley et al. 2000).

Goicoechea. J.R., et al., 2017, A&A 601, L9

The ALMA view of the Orion Bar

Table D.1. Timescales, in hours, for chemical destruction by reactive collisions with H_2, H, e^- and by FUV photodissociation.

Ion	$\tau(H_2)^a$	$\tau(H)^a$	$\tau(e^-)^a$	$\tau(\text{photodiss.})^b$
CH^+ $\tau_D \approx$ **4 h**[c]	$4.6\,h\,(10^5\,cm^{-3}/n_H)\,f_{H_2}^{-1}$	$3.7\,h\,(10^5\,cm^{-3}/n_H)\,(1-f_{H_2})^{-1}$	$185\,h\,(10^5\,cm^{-3}/n_H)\,(10^{-4}/x_e)$	$84.2\,h\,e^{+2.94 A_V}$
HOC^+ $\tau_D \approx$ **26 h**[c]	$14.6\,h\,(10^5\,cm^{-3}/n_H)\,f_{H_2}^{-1}$	—	$252\,h\,(10^5\,cm^{-3}/n_H)\,(10^{-4}/x_e)$	$5144\,h\,e^{+3.32 A_V}$
SH^+ $\tau_D \approx$ **46 h**[c]	—	$25\,h\,(10^5\,cm^{-3}/n_H)\,(1-f_{H_2})^{-1}$	$111\,h\,(10^5\,cm^{-3}/n_H)\,(10^{-4}/x_e)$	$111\,h\,e^{+1.66 A_V}$
SO^+ $\tau_D \approx$ **73 h**[c]	—	—	$139\,h\,(10^5\,cm^{-3}/n_H)\,(10^{-4}/x_e)$	$27.8\,h\,e^{+1.70 A_V}$

Notes. [a] Assuming $T_k = T_e = 300$ K. [b] For a FUV-radiation field of $\chi = 10^4$. [c] Total destruction timescale (τ_D) at $A_V = 1$ assuming $n_H = 10^5\,cm^{-3}$ and $f_{H_2} = 0.5$. For CH^+ (HOC^+), τ_D is shorter (longer) than the timescale for non-reactive collisions in their low-lying rotational levels (see Table D.2.).

Goicoechea. J.R., et al., 2017, A&A 601, L9

WISH: Constraints on low-mass to high-mass protostars

	NGC 1333 2A	NGC 1333 4A	NGC 1333 4B	Ser SMM 1	L 1489	NGC 7129 FIR2	W3 IRS5	NGC 6334 I	NGC 6334 I(N)	AFGL 2591	S 140	NGC 7538 IRS1
CH^+	N blue	M blue	M blue	M blue		M red	M pcyg	M red	N red	M pcyg	N blue	M ipcyg
OH^+		M blue	M blue	M blue		M red	M pcyg	M b+r	M red	M pcyg	M red	M red
H_2O^+				M blue			M blue			M blue		N blue
H_3O^+							M red	N blue	M red	M red	N red	
SH^+							M blue					
HCO^+	M blue	M blue	M blue	M blue	M blue	M red	M red	M blue	M red	M blue	M red	M blue
C^+	M blue	M blue		M blue			M pcyg			M pcyg	M blue	
CH	N ipcyg	N ipcyg	N ipcyg	M+N ipcyg		M red	N red	N ipcyg	N red	N red	N red	N blue

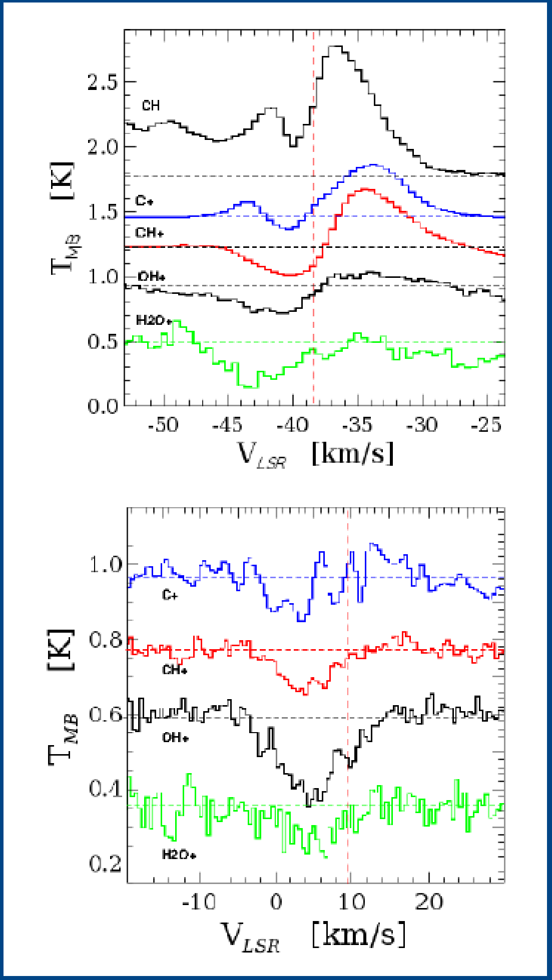

Benz., A., et al. 2016, A&A 590, 105

WISH: Constraints on low-mass to high-mass protostars

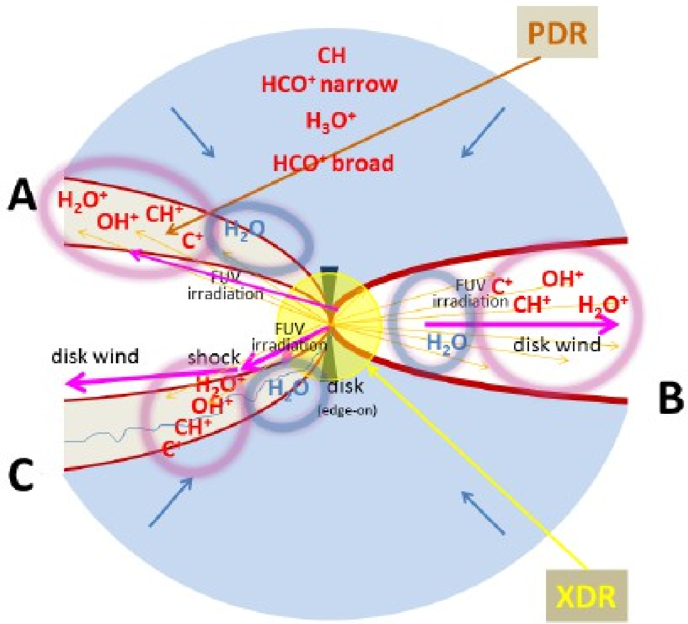

Fig. 10. Cartoons of three scenarios described in the text for the origin of the observed CH^+, OH^+, H_2O^+, and C^+ absorptions. *A:* Irradiated outflow walls with slow shocks entraining the outer layers of the walls; *B:* disk wind irradiated by protostellar FUV; *C:* fast dissociative shocks irradiated by protostellar FUV.

Low mass stars: a high FUV luminosity ($1.5\ L_{sun}$) is required to explain observations.

High mass stars: The estimated UV flux is lower than that predicted at the distance of the Herschel beam. Extinction by a circumstellar disk?

Benz., A., et al. 2016, A&A 590, 105

Star forming regions (dust)

Monoceros R2 (HOBYS, PI: F. Motte)

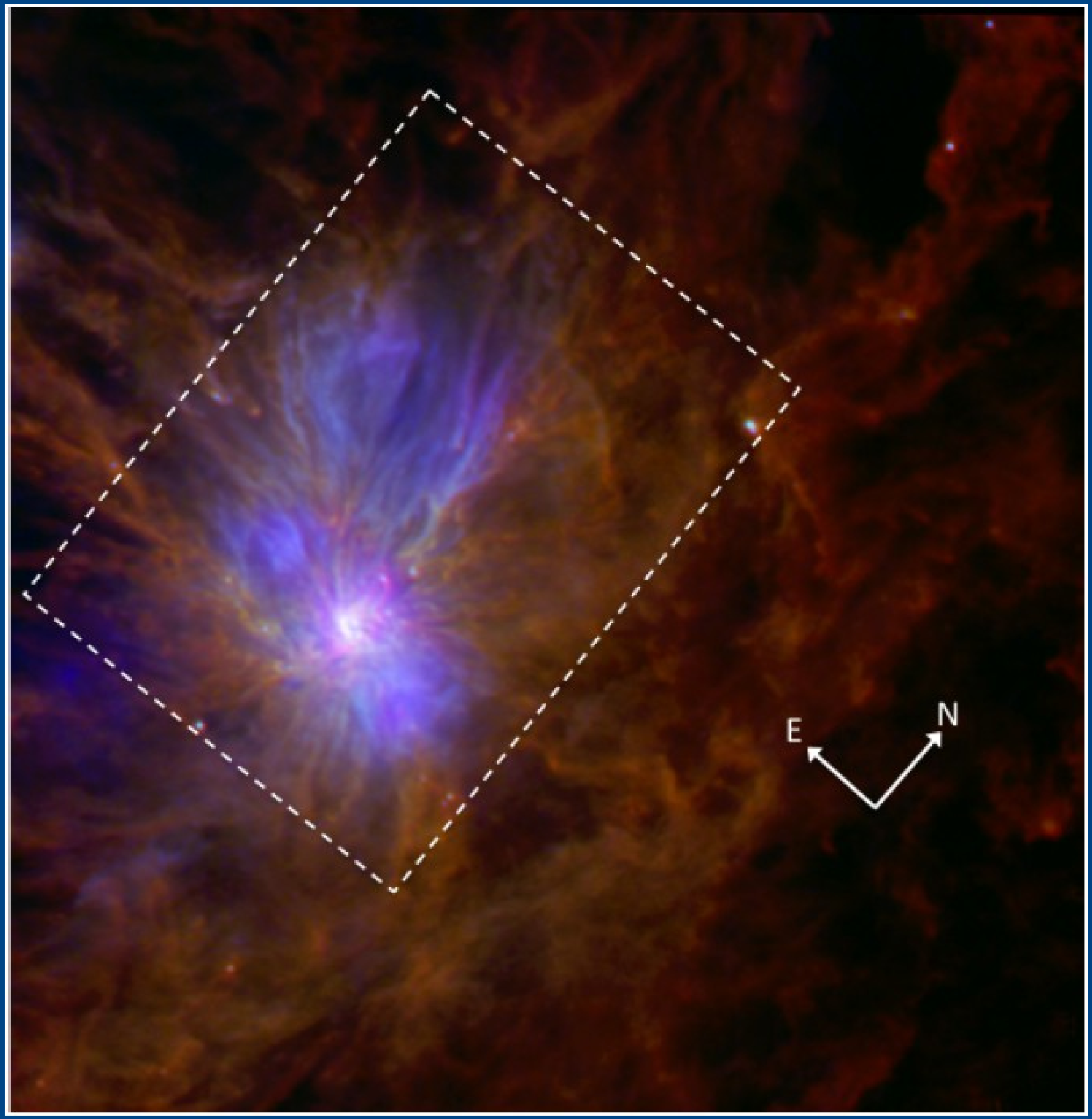

PACS+SPIRE

70 µm (blue)
160 µm (green)
250 µm (red)

Monoceros R2

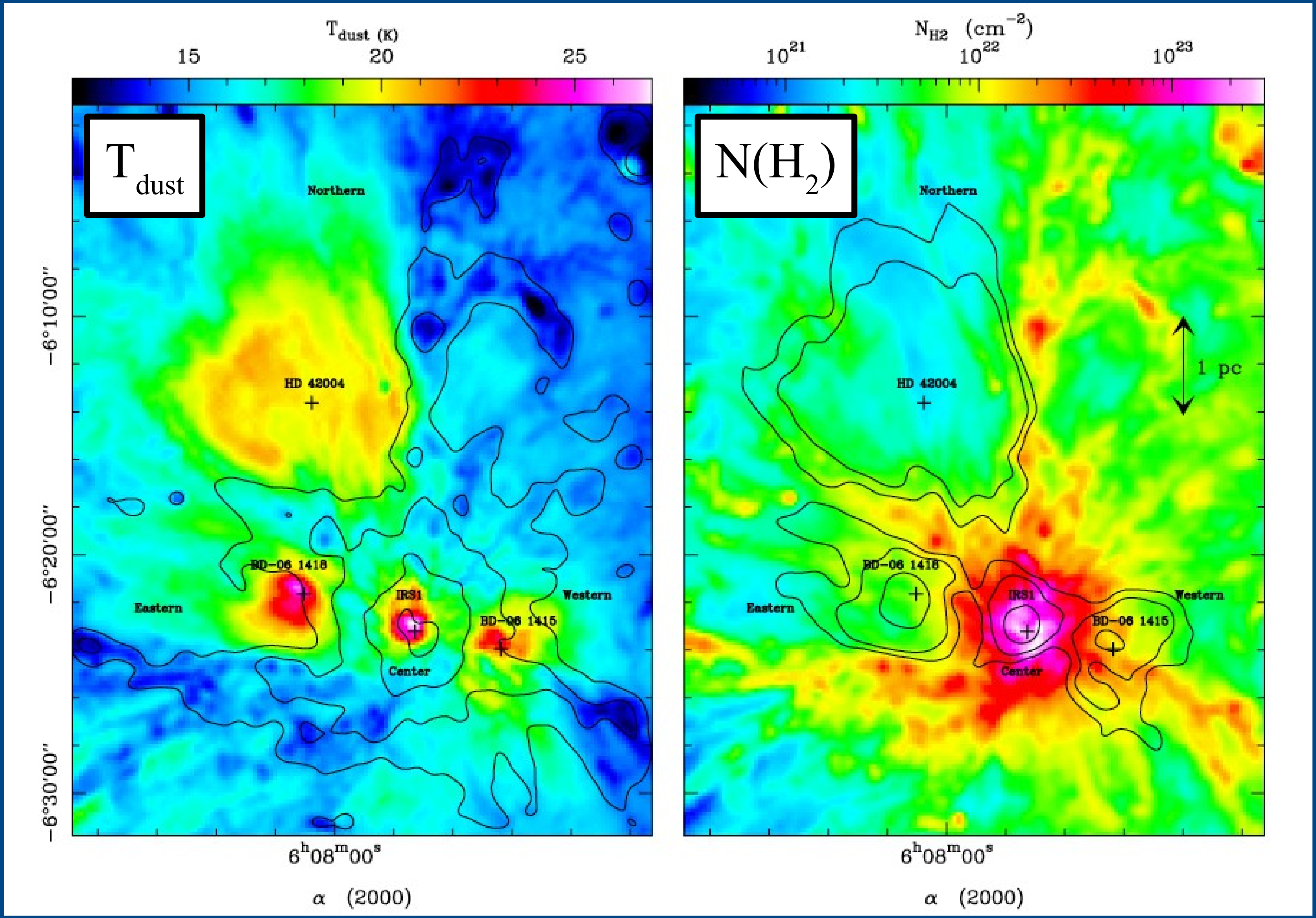

Didelon, P,, Motte, F, Tremblin, P. et al. A&A, submitted

Monoceros R2

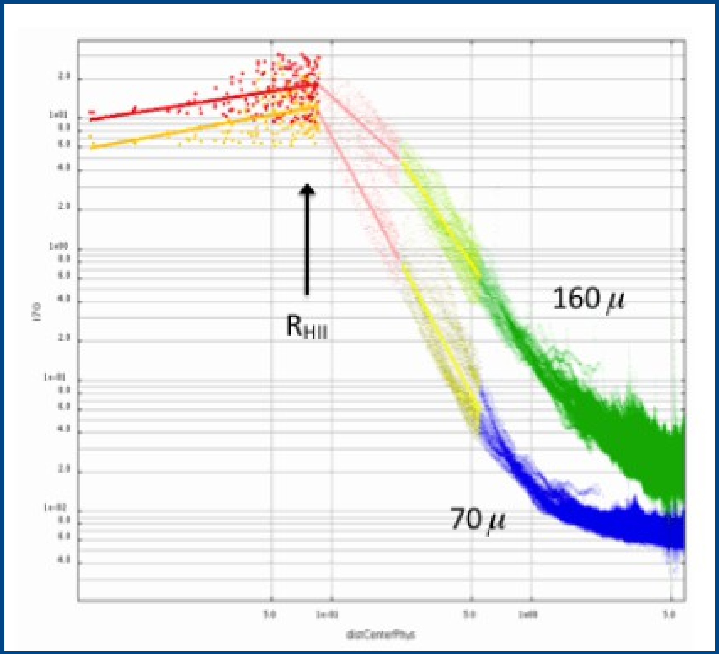

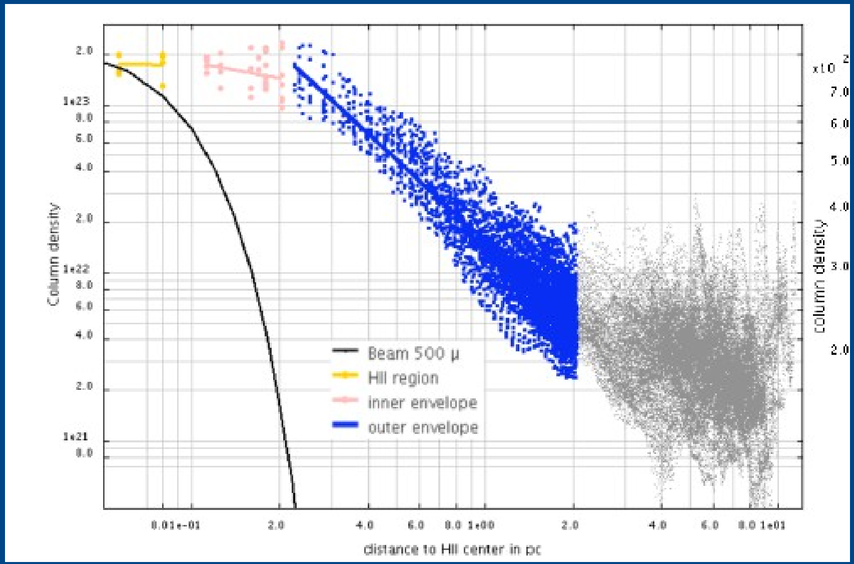

Table 3: Properties of the neutral envelopes surrounding the four H II regions of Mon R2

Region name	$R_{\rm Infall}$ [pc]	$R_{\rm out}$ [pc]	$\rho(r) \propto r^q$ $q_{\rm in}$	$q_{\rm out}$	Infall age [Myr]	$N_{\rm H2}^{\rm Max}$ [cm^{-2}]	$R_{\rm HM}$ [pc]	$\langle\rho_{\rm obs}\rangle$ [cm^{-3}]	$\rho_{\rm env}$(1pc) [cm^{-3}]	$\rho_{\rm env}(R_{\rm H\,II})$ [cm^{-3}]
(1)	(2)	(3)	(4)	(5)	(6)	(7)	(8)	(9)	(10)	(11)
central	$.3 \pm .1$	$2.5 \pm .5$	$-.85 \pm .35$	-2.7	$.5 - 1.5$	$2. \times 10^{23}$	0.35	1.4×10^5	2000 ± 300	1.5×10^5
western	$.5 \pm .1$	$3. \pm 1.$	$-1.5 \pm .15$	-1.8	.8–2.5	$16. \times 10^{21}$	0.4	$9. \times 10^3$	350 ± 50	12000
eastern	$.9 \pm .2$	$2.5 \pm 1.$	$-.4 \pm .2$	-2.3	1.4–4.4	$7. \times 10^{21}$	0.9	$1.6. \times 10^3$	450 ± 50	1200
northern	> 2	$2.5 \pm .5$	$-1.45 \pm .15$	-	$> 3.–10.$	$3. \times 10^{21}$	1.5	300.	115 ± 30	150

Didelon, P, Motte, F, Tremblin, P. et al. 2015, A&A 584, 4

Monoceros R2

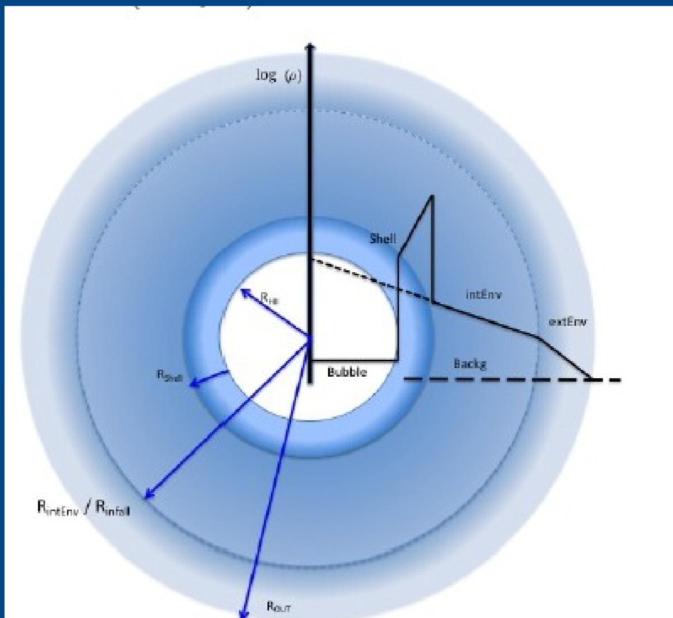

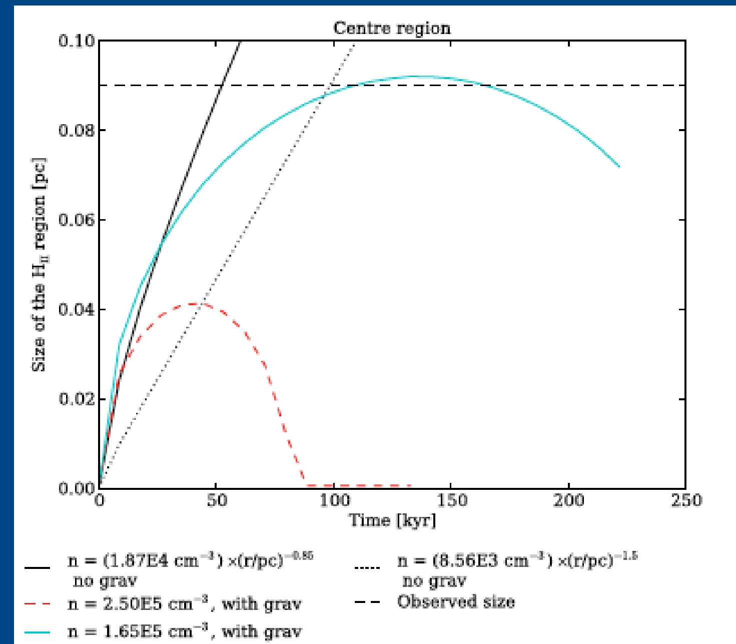

Table 4: Estimations of expansion time for the four H II regions of Mon R2

Region	Analytical calculations and simulations without gravity					Simulations with gravity			Adopted
	Constant density		Decreasing density			Constant density		Dec.density	expansion
	$\langle\rho_{\rm initial}\rangle$ [cm^{-3}]	$t_{\rm Spitzer}$ [kyr]	ρ_c [cm^{-3}]	$t_{\rm exp}$ (calc) [kyr]	$t_{\rm exp}$ (simu.) [kyr]	$\langle\rho_{\rm initial}\rangle_{\rm Max}$ [cm^{-3}]	$t_{\rm exp}$ (simu) [kyr]	$t_{\rm exp}$ (simu) [kyr]	time [kyr]
(1)	(2)	(3)	(4)	(5)	(6)	(7)	(8)	(9)	(10)
central	2×10^5	54	2×10^6	58	53	1.7×10^5	133	-	90 ± 40
western	2.4×10^4	92	1×10^6	108	98	1.7×10^4	215	-	150 ± 50
eastern	1.5×10^3	23	4×10^3	24	23	8×10^3	170	24	25 ± 5
northern	3×10^2	310	2.5×10^5	370	355	5×10^3	3700.	370	350 ± 50

Didelon, P, Motte, F, Tremblin, P. et al. 2015 A&A, 584, 4

The global dust SED

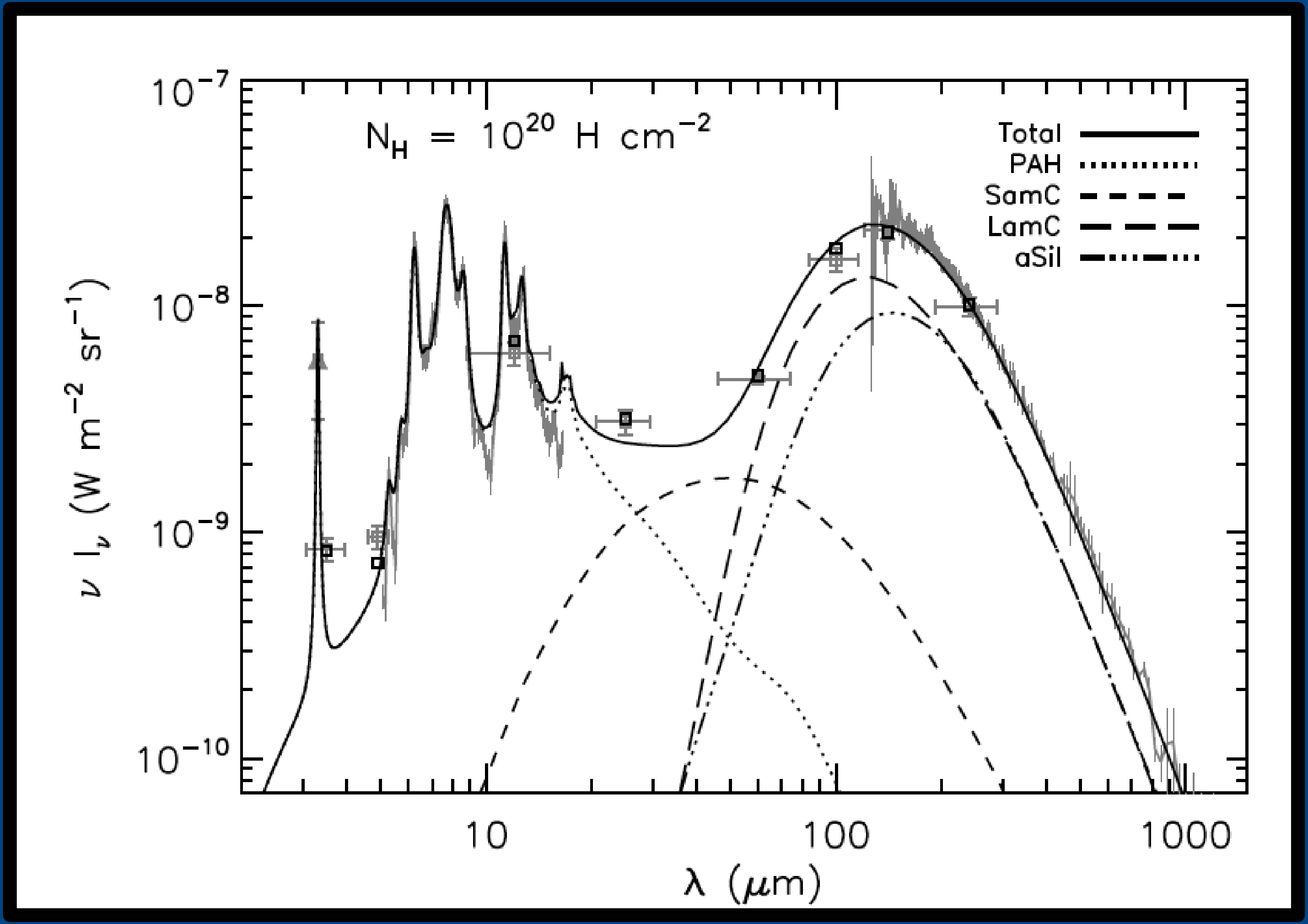

DustEM

DHGL (Diffuse interstellar medium at High Galactic Latitude)

Compiègne M., Verstraete L., Jones A. et al. 2011, A&A 525, 103

The global dust SED

Table 2. DHGL dust model abundances and size distribution parameters (see §4.2). Y is the mass abundance per hydrogen for each dust component. $f_{M_{tot}}$ is the dust component mass as a fraction of the total dust mass.

	σ	a_0 (nm)			Y (M/M_H)	$f_{M_{tot}}$
PAH	0.1	0.64			$7.8\ 10^{-4}$	7.7%
SamC	0.35	2.0			$1.65\ 10^{-4}$	1.6%
	α	$a_{\rm min}$ (nm)	a_c, a_t (nm)	γ		
LamC	-2.8	4.0	150	2.0	$1.45\ 10^{-3}$	14.2%
aSil	-3.4	4.0	200	2.0	$7.8\ 10^{-3}$	76.5%
				TOTAL	$10.2\ 10^{-3}$	

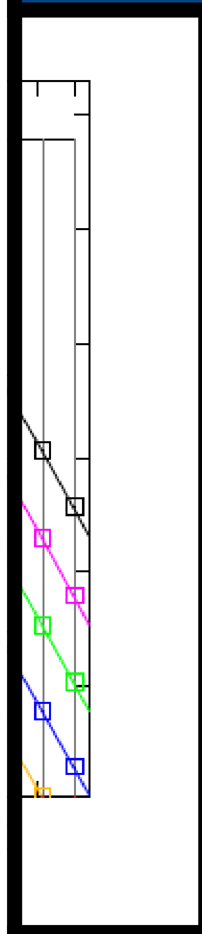

DHGL (Diffuse interstellar medium at High Galactic Latitude)

Compiègne M., Verstraete L., Jones A. et al. 2011, A&A 525, 103

Dust evolution in the Orion Bar

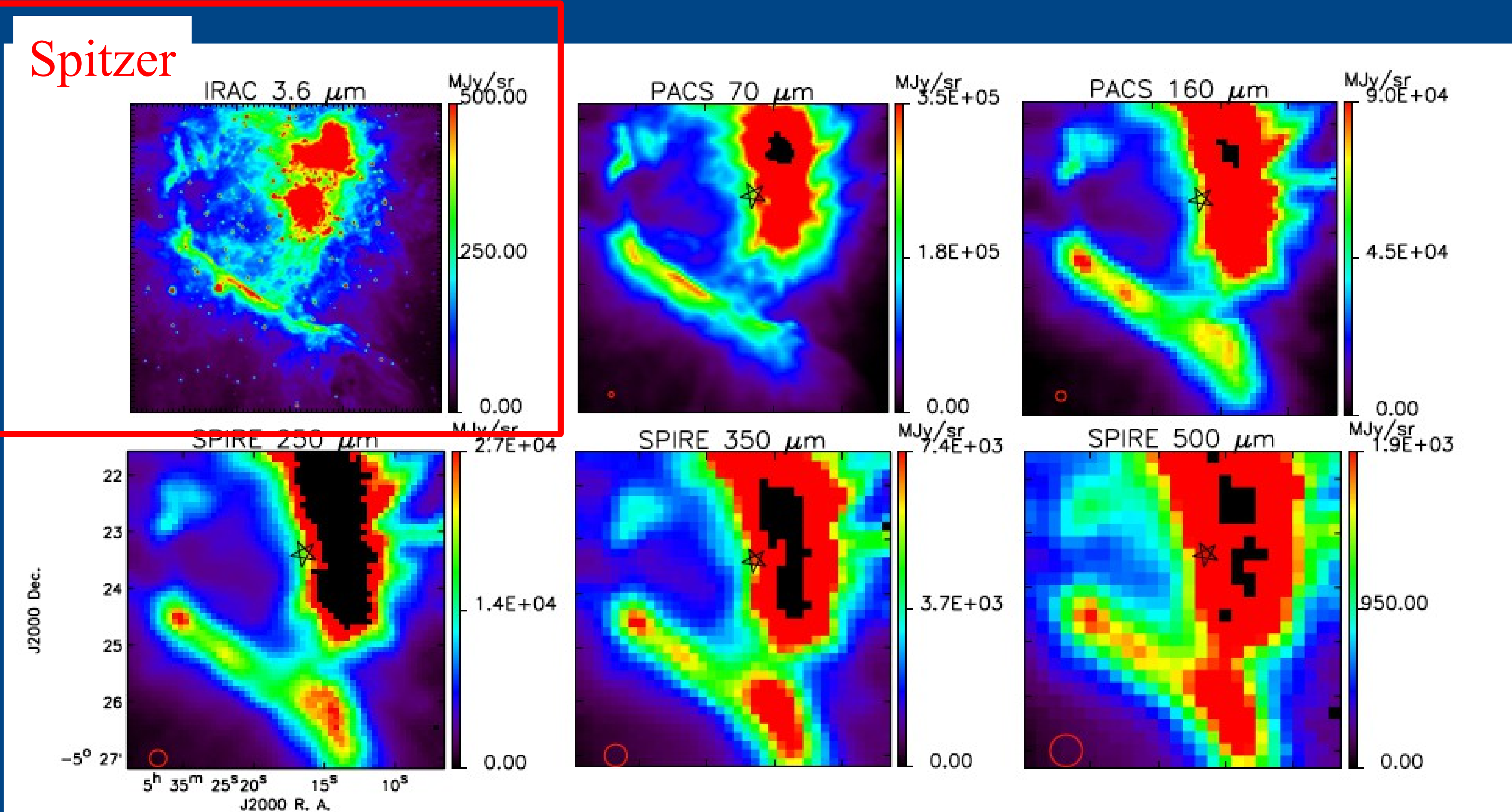

Fig. 1. Orion bar maps observed by IRAC, PACS and SPIRE instruments. The red circle bottom right stands for the FWHM for each channel, and the black star shows the location of the illuminating source. The saturated pixels are indicated in black.

Arab, H., Abergel, A., Habart, E., 2012, A&A 541, 19

Dust evolution in the Orion Bar (DustEM+DHGL)

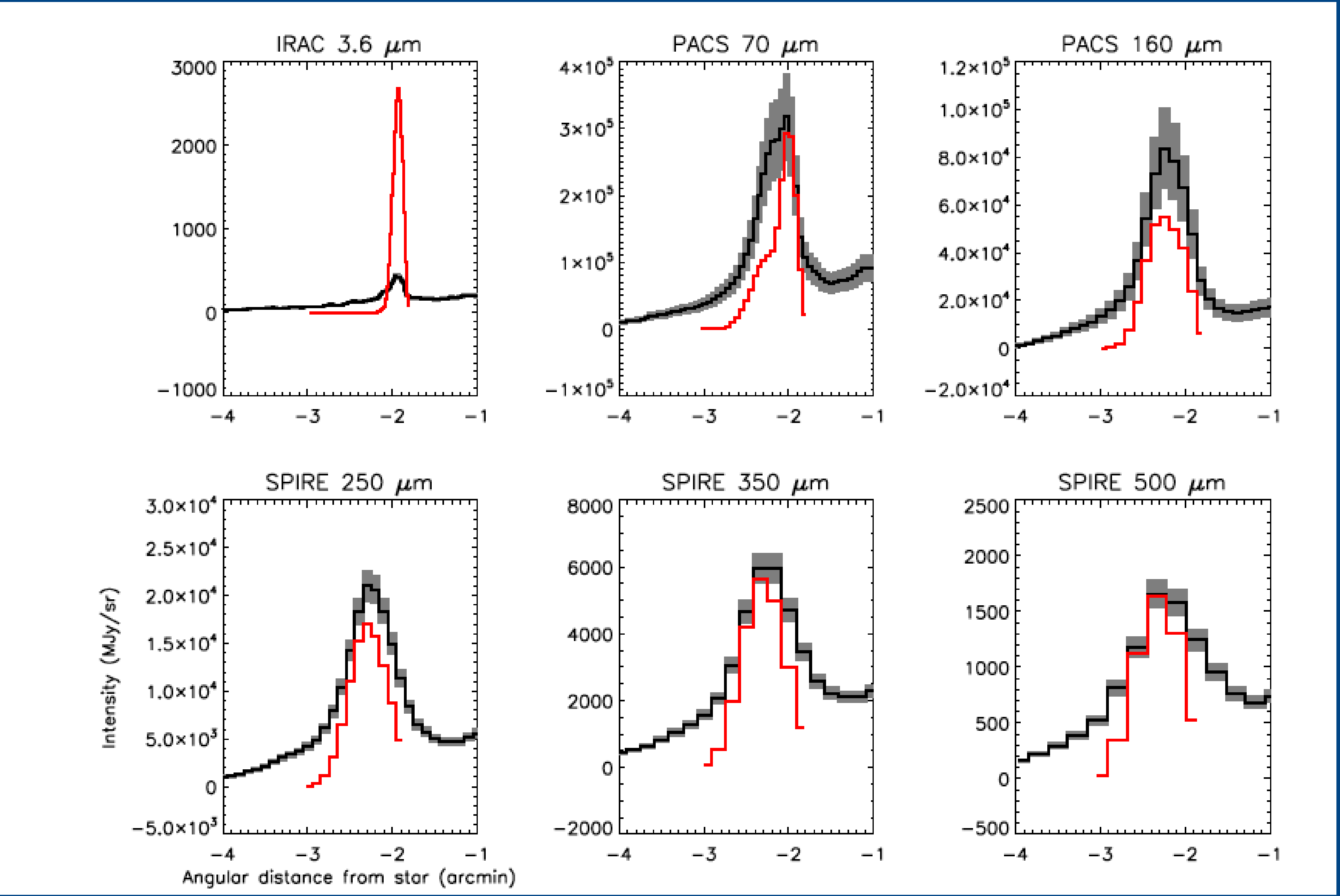

Arab, H., Abergel, A., Habart, E., 2012, A&A 541, 19

Dust evolution in the Orion Bar (DustEM+PAH depleted model)

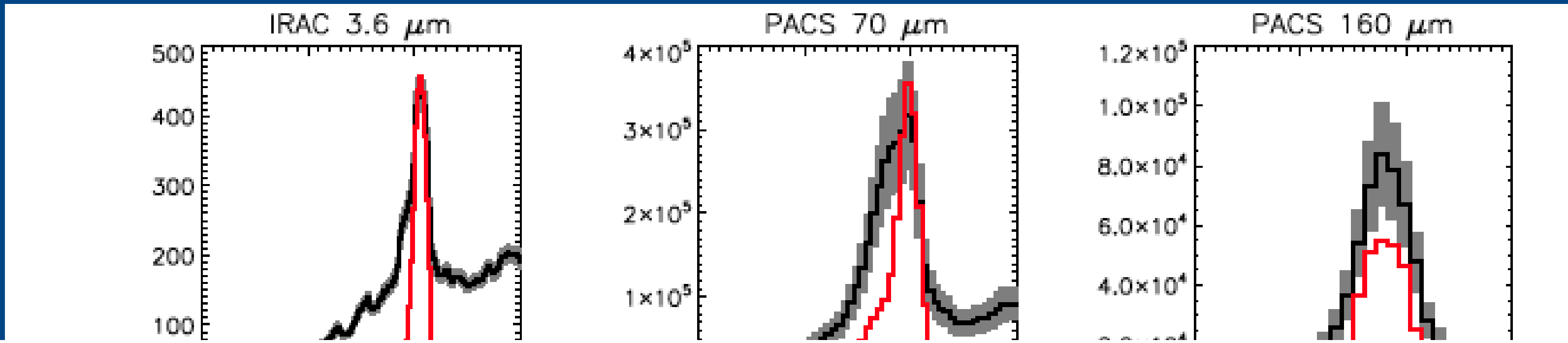

	Y_{PAH} (M/M_H)	Y_{SamC}	Y_{LamC}	Y_{aSil}	ϵ_{FIR}	l_{PDR} (pc)
Diffuse ISM model (Fig. 9)	7.8×10^{-4}	1.65×10^{-4}	1.45×10^{-3}	7.8×10^{-3}	$\epsilon^0_{FIR}(\lambda)$ [a]	0.45
PAH depleted model (Fig. 10)	1.1×10^{-4}	1.65×10^{-4}	1.45×10^{-3}	7.8×10^{-3}	$\epsilon^0_{FIR}(\lambda)$ [a]	0.45
PAH depleted model + ϵ_{BG} enhancement (Fig. 11)	2.36×10^{-4}	1.65×10^{-4}	1.45×10^{-3}	7.8×10^{-3}	$2 \times \epsilon^0_{FIR}(\lambda)$ [a]	0.25

Notes. [(a)] $\epsilon^0_{FIR}(\lambda)$ is the FIR emissivity presented in Fig.A1 from Compiègne et al. (2011).

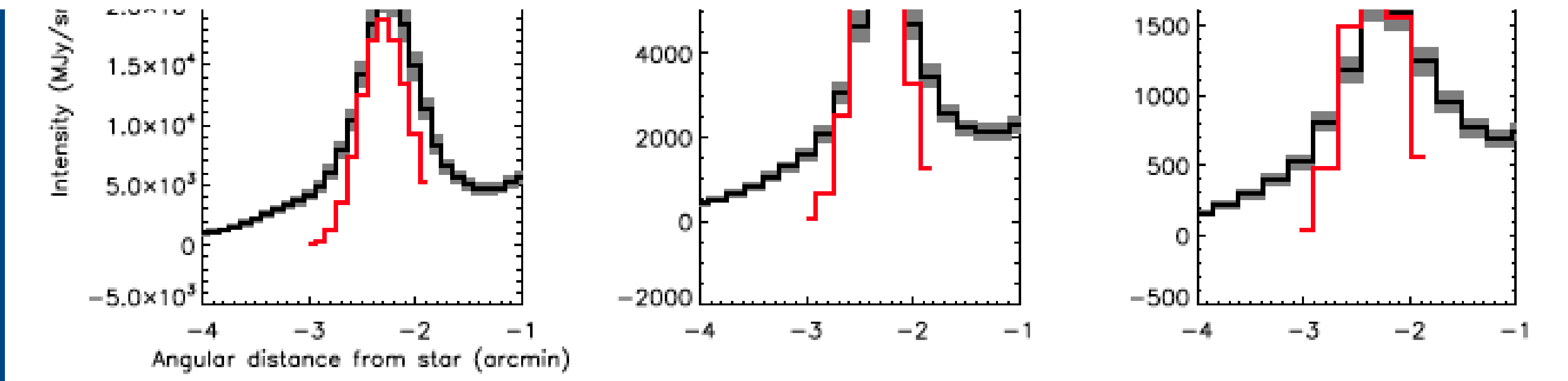

Arab, H., Abergel, A., Habart, E., 2012, A&A 541, 19

Bimodal dust distribution in IC 434

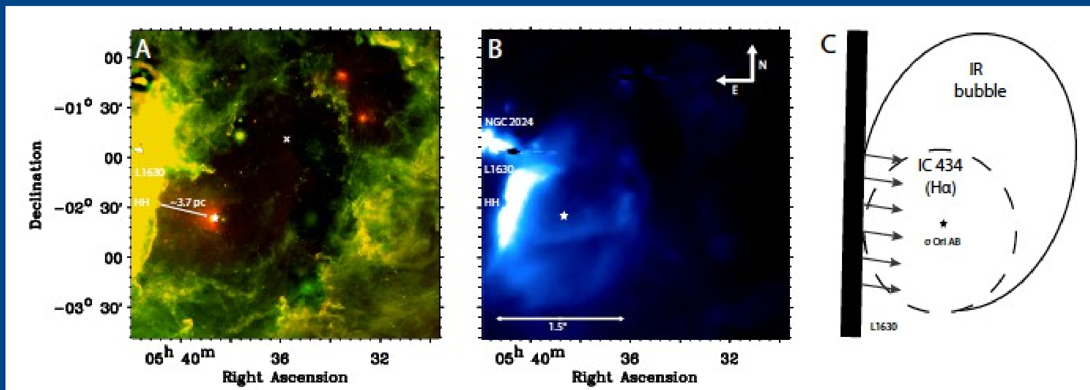

WISE 12 μm and 22 μm

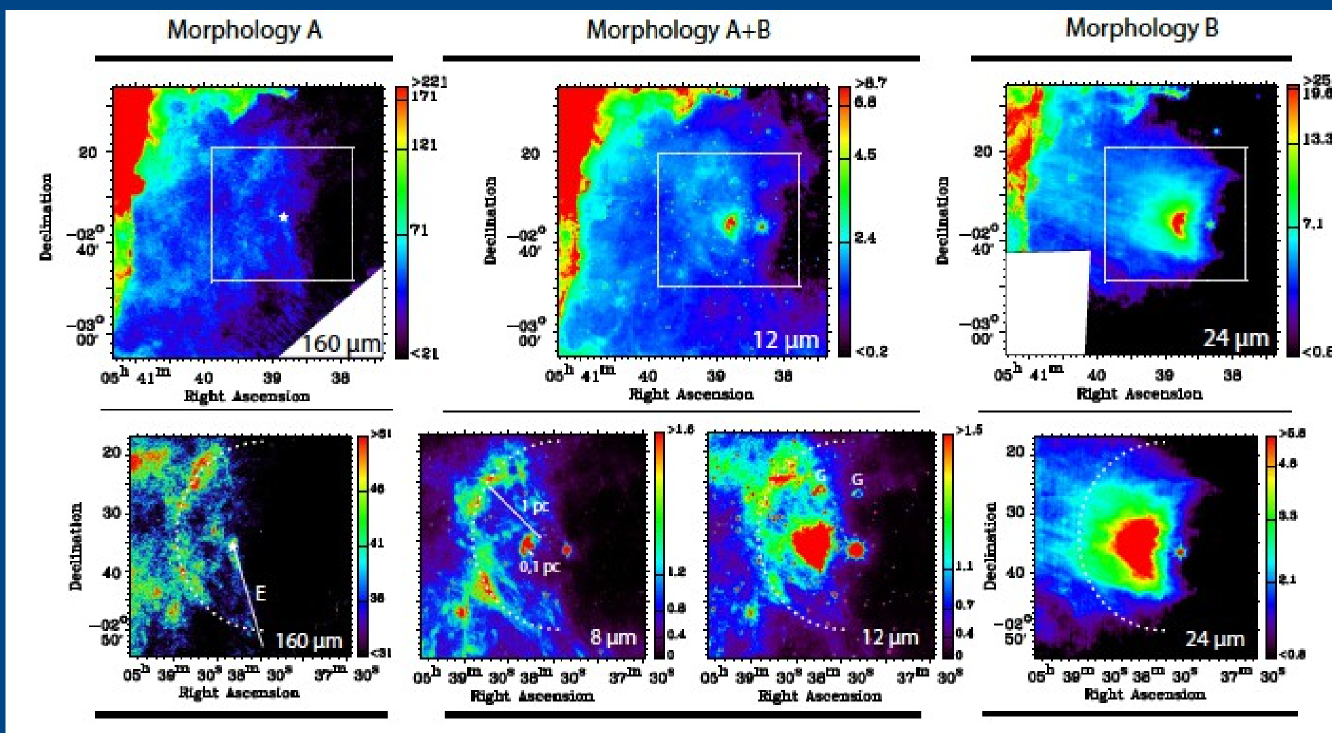

Spitzer
+
HERSCHEL

Ochsendorf & Tielens, 2015, A&A 576, 2

Bimodal dust distribution in IC 434

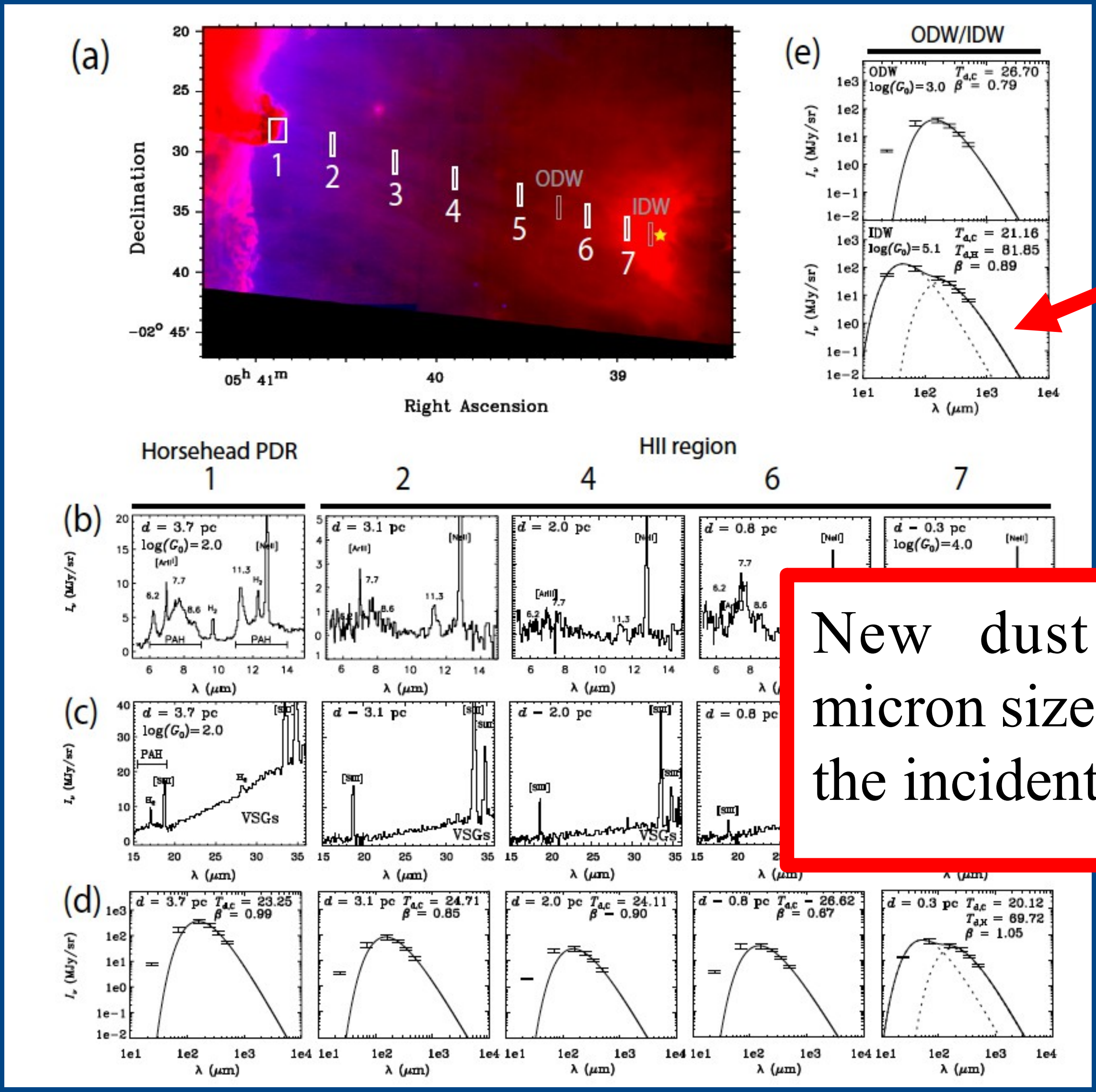

Two different dust components

New dust population. Fluffy micron sized grains, insensitive to the incident radiation field.

Ochsendorf & Tielens, 2015, A&A 576, 2

Towards Xgal

[CII] in the Orion Molecular Cloud

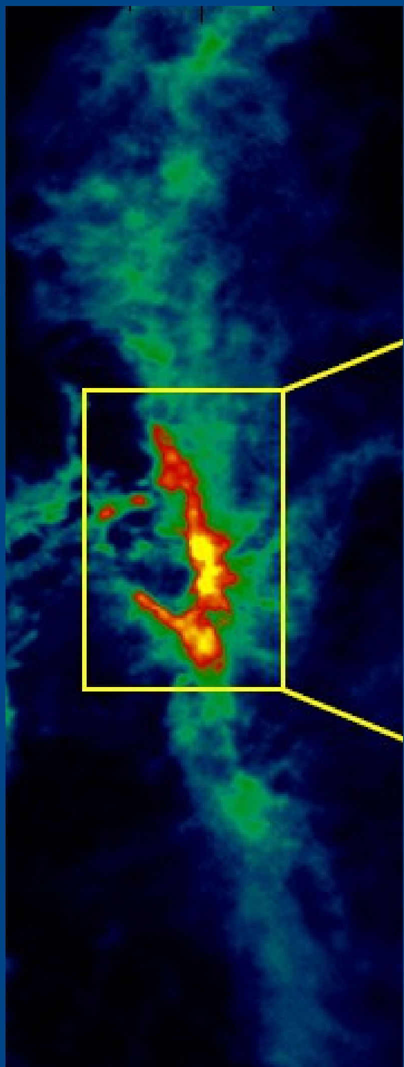

Orion Molecular Cloud-1 (OMC1)

8’ x 12’ (0.9pc x 1.4pc)
(OT1_jgoicoec_4)

13CO J=2-1, IRAM-30m @ 11’’ (Berné et al. 2014)

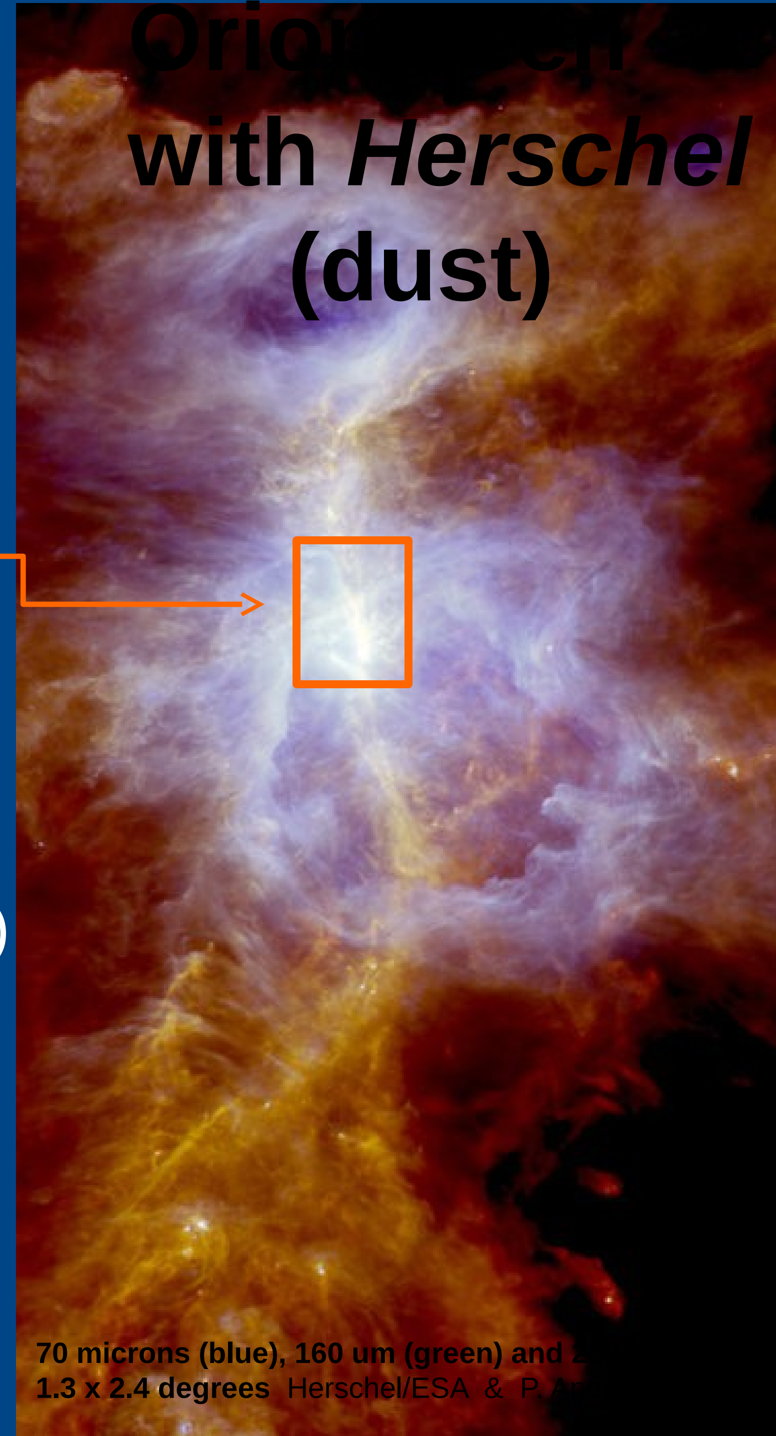

[CII]/L_{FIR} in Xgal

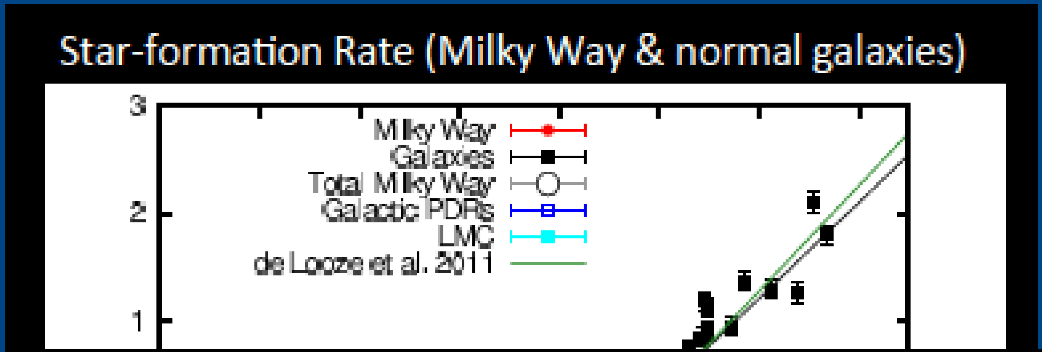

[CII] is a good SFR tracer in nearby galaxies.

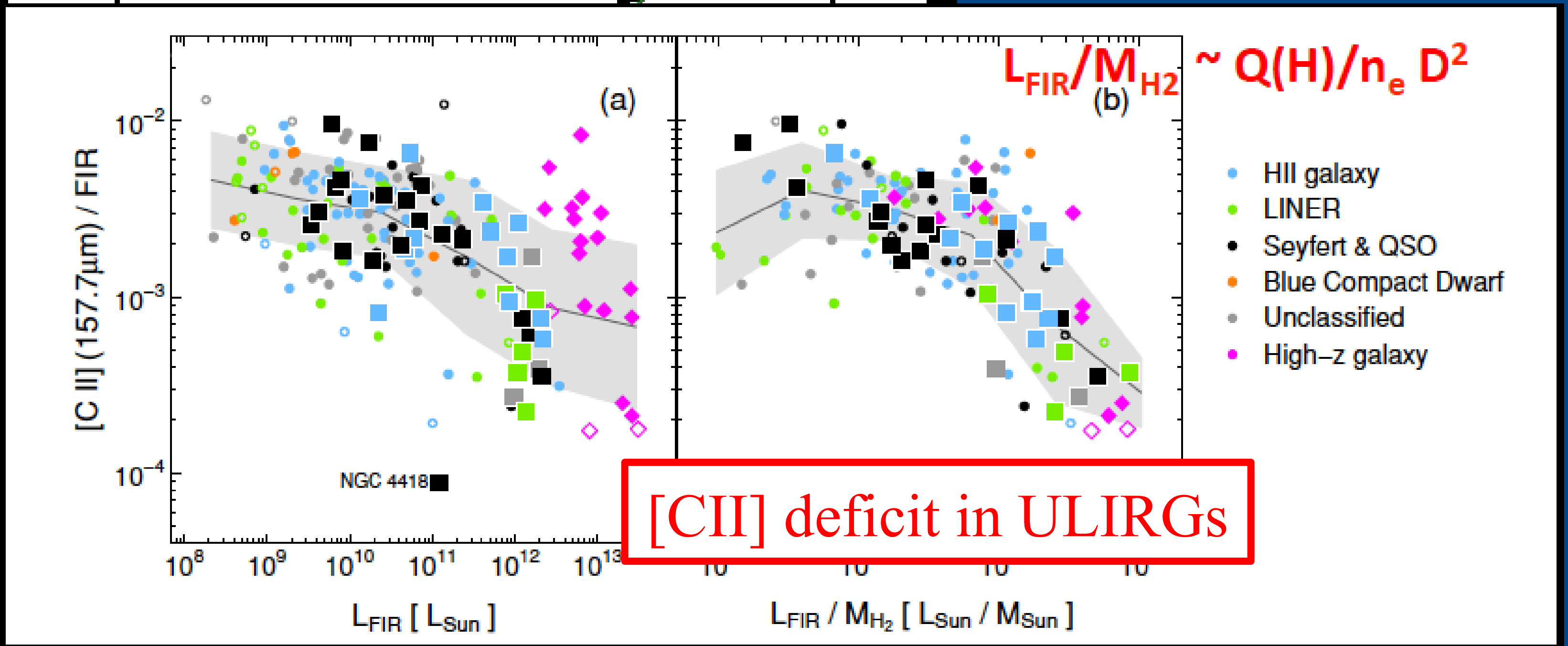

Graciá-Carpio+2011, ApJ 728,7

[CII] in Orion

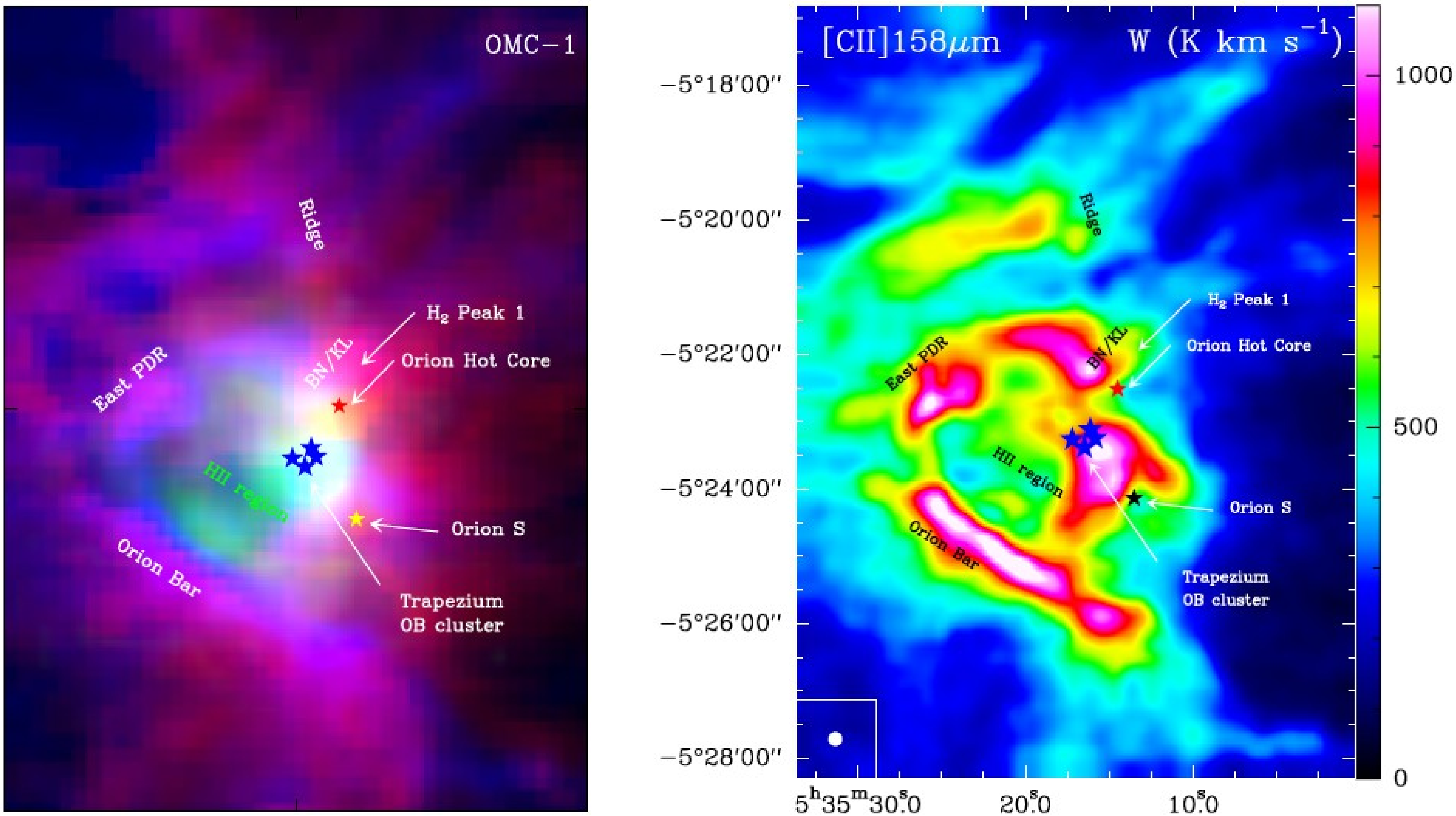

Figure 1. (Left): Composite image with the H41α (green), [C II] 158 μm (blue) and CO 2-1 (red) integrated intensities. The position of the main sources in Orion are shown. (Right): *Herschel*/HIFI map of the continuum-subtracted [C II] 158 μm line (integrated intensity from 0 to 17 km s^{-1}).

Goicoechea, Teyssier, Etxaluze et al., 2015, ApJ 812, 75

[CII] in Orion

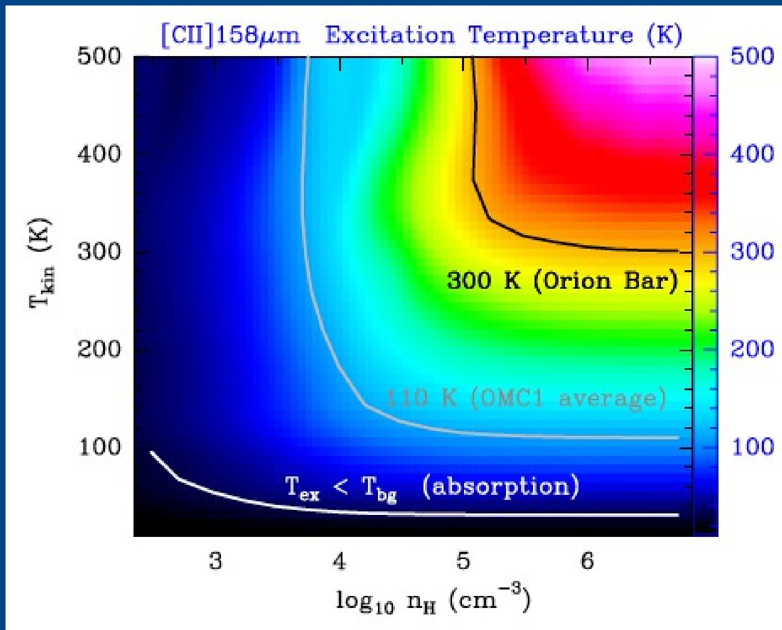

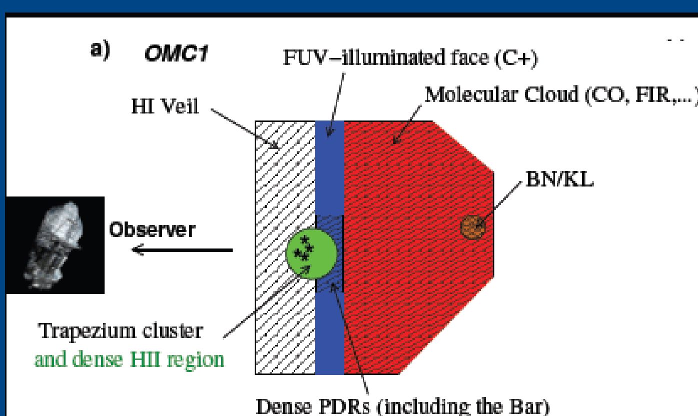

- Non-local, non-LTE grid:

  - $\tau = \tau_{[CII]} + \tau_{dust}$ (160µm)
  - FIR pumping (strong background)
  - Line-trapping and broadening

Extended OMC1 face:

$T_{ex} > 110$ K

$\rightarrow n_H > 5000$ cm^{-3}

Dense PDRs (Bar, Trapezium,

$T_{ex} > 300$ K $\rightarrow$ $n_H > 10^5$ cm^{-3}

85 %

Goicoechea, Teyssier, Etxaluze et al.,, 2015, ApJ 815, 75

[CII]/L_{FIR} in Orion

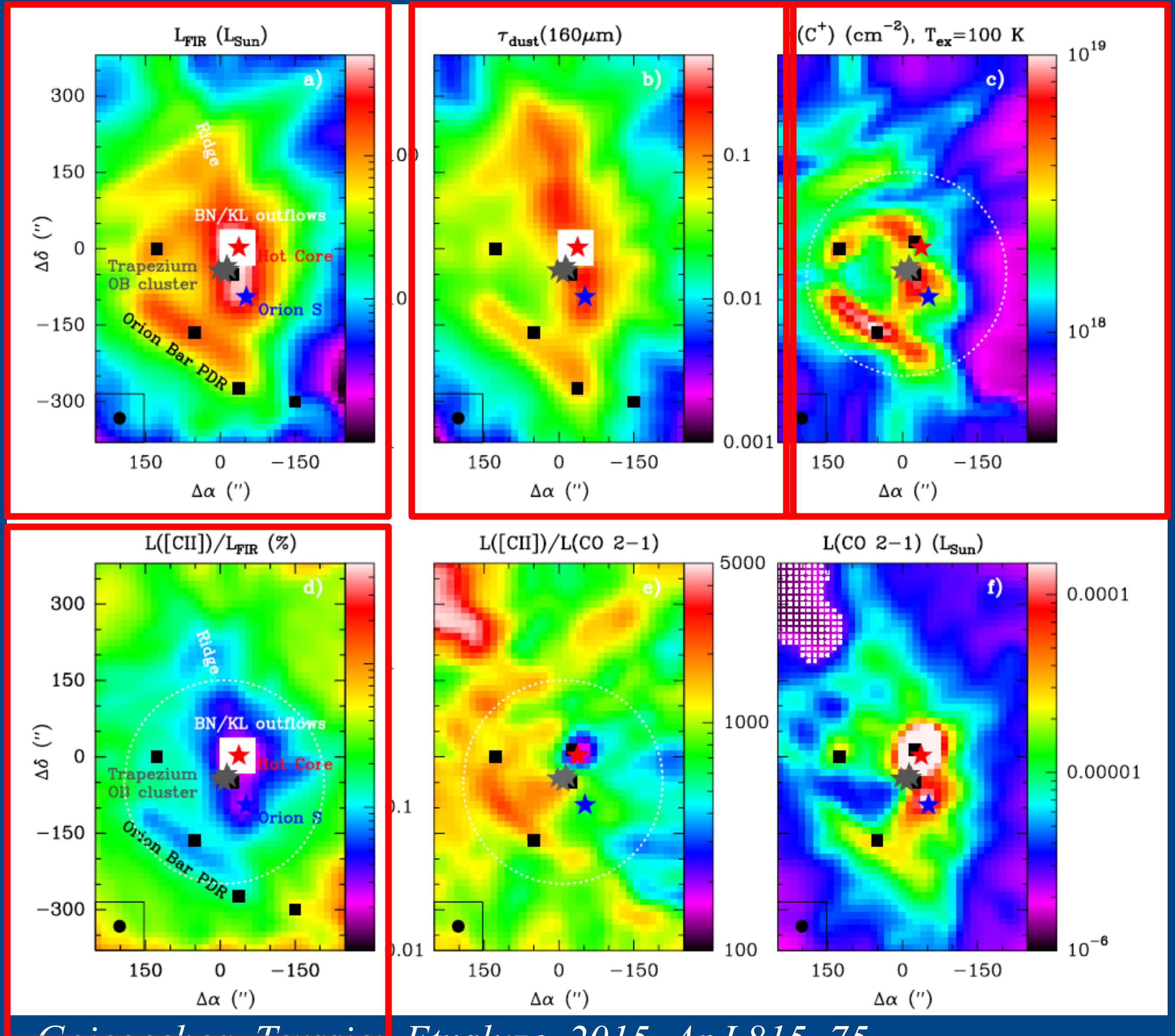

Goicoechea, Teyssier, Etxaluze, 2015, ApJ 815, 75

[CII]/L_{FIR} in Orion

Table 1
Average physical parameters in OMC 1

	L_{C^+}/L_{FIR}	$L_{CO\,2-1}/L_{FIR}$	$L_{C^+}/L_{CO\,2-1}$	L_{FIR}/M_{Gas} ($L_\odot/M_\odot$)	G_0^b (Habing field)	$\tau_{d,160}$
OMC 1 .... (full map[a])	3.1×10^{-3}	3.6×10^{-6}	1100	54	7.5×10^3	0.03
Near Trapezium .... (R<0.4 pc[a])	1.0×10^{-3}	1.2×10^{-6}	1000	77	1.9×10^4	0.06
Extended Cloud .... (R>0.4 pc)	3.8×10^{-3}	4.5×10^{-6}	1150	45	3.3×10^3	0.02

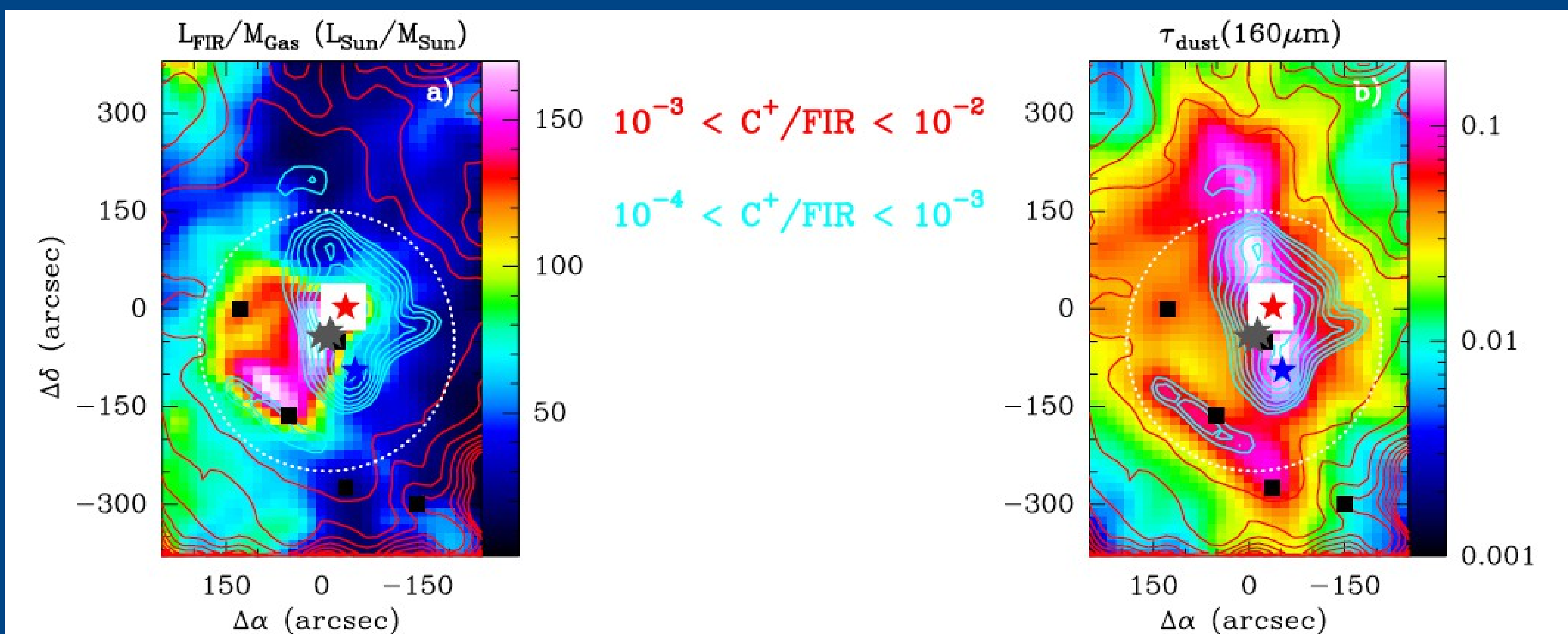

Goicoechea, Teyssier, Etxaluze et al., 2015, ApJ 815, 75

[CII]/L_{FIR} in Xgal vs Orion

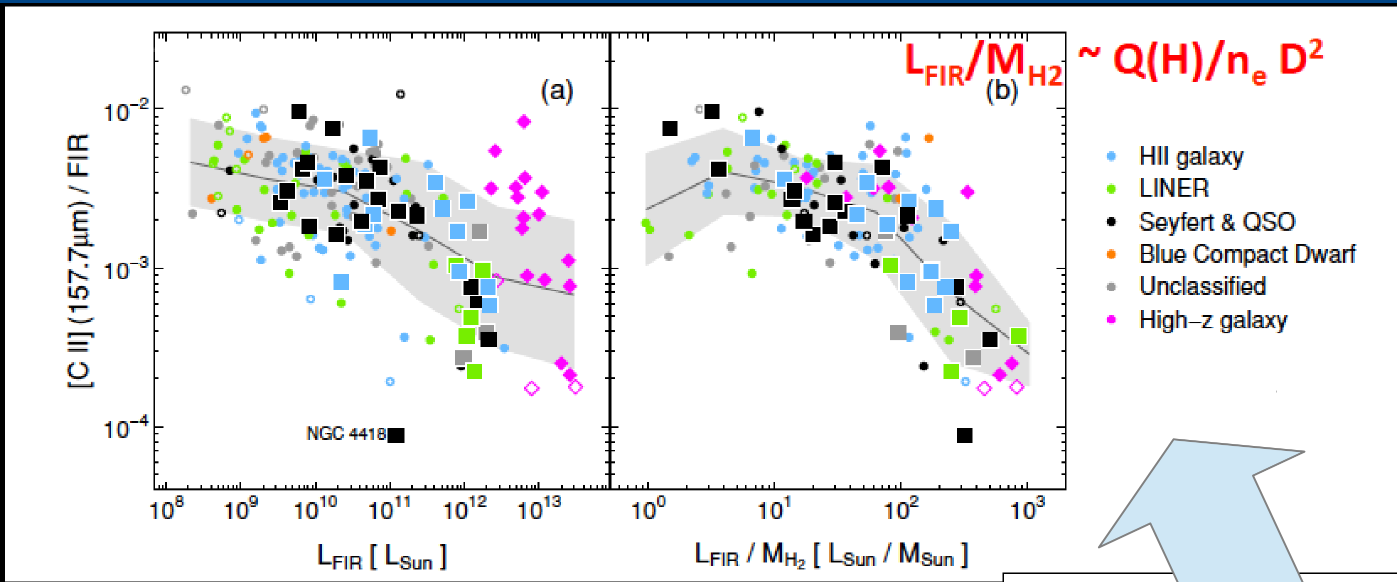

Graciá-Carpio+2011, ApJ 728,7

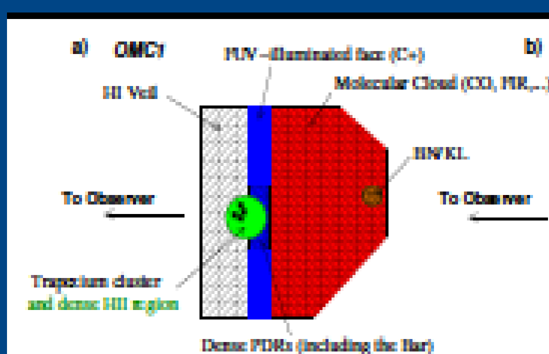

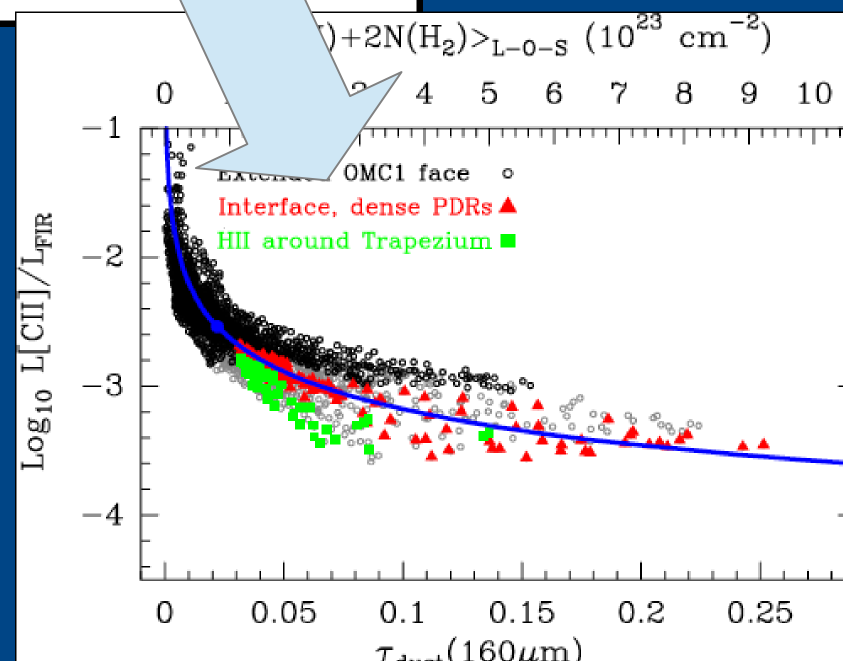

Summarizing...

Spitzer and Herschel have provided a first insight into the physics and chemistry of the gas and dust in PDRs. Current models offers a reasonable overall picture of PDRs but present some deficiencies for the external layers Av < 2 mag.

i) Reactive ions as a probe of external layers of PDRs.

ii) Chemistry + excitation need to be coupled in the warmest layers of the PDR where very reactive ions survive.

iii) Dust composition is essential for chemical models.

iv) Galactic PDRs as Xgal patterns.